Politecnico di Torino

Department of Aerospace Engineering

Master Thesis

Investigation on advanced materials of plasma sources for plasma antenna applications

Candidate:
Fadda Paola

Supervisor:
prof. Lorenzo Casalino

TECHNOLOGY FOR PROPULSION AND INNOVATION

Tutor:
dr. Marco Manente

October 2019

Contents

List of Tables

List of Figures

Abstract

Gaseous Plasma Antennas are devices which rely on a partially or fully ionized gas to radiate EM waves, thus differing from the traditional antenna design that is based on metallic wires and/or surfaces. Gaseous Plasma Antennas consist of dielectric vessel filled with a neutral gas such as argon that is energized by any generation method to form plasma. A metal circuit is wrapped around the tube or in contact with the plasma itself to inject the signal frequency into the plasma. Plasma antennas might offer several advantages with respect to conventional antennas, e.g. electrical frequency reconfigurability, making them suitable for space communications. The plasma antennas performances, e.g. gain, are related to the discharge parameters, in particular the plasma density is the parameter on which this work is focused on.

In this study, the use of different materials to increase the plasma density, and consequentially the antenna gain, is investigated. The external casing of the plasma sources is made of glass. To improve the electron density value of a Gaseous Plasma Antenna in the same working conditions, many attempts have been made in replacing or coating the glass with different materials. These materials are characterized by a high value of Secondary Electron Emission Yield. The Sol-Gel method is used to make a thin film and the procedures to realize the coatings are described. The Scanning Electron Microscope images and the profilometer analysis to investigate the morphology and the thickness of the deposited layers are shown.

By means of a microwave interferometer, the plasma density is measured. Data analysis and results of the experiments are presented, showing that the materials derived from the literature are indeed applicable to plasma antennas to increase the plasma density.

CHAPTER 1

Introduction

1.1 Plasma Properties

Plasma is defined as an ionized gas, meaning that the atoms are dissociated into positive ions and negative electrons. However, not every cloud of ionised gas is plasma. A plasma is a quasineutral gas of charged and neutral particles which exhibits collective behaviour [1].
In other words, a plasma is an ensemble of ions, and electrons in equal number (quasineutrality), together with neutral particles, whose physic, and motion are mostly governed by electromagnetics, rather than collisions as in a neutral gas (collective behavior) [1].

The matter at thermodynamic equilibrium ($T \geq 10^4 K$) reaches spontaneously the plasma state when the thermal agitation has enough energy to ionize. Otherwise, for systems which are not at thermodynamic equilibrium, exciters agents, as photons or stream of particles, can be used. In general, if enough power is supplied to a collection of gas particles it leads to the ionization of a fraction of them. In an ionized gas, the specie (ions, electrons, or neutrals) density n_ξ is defined as the number of particle of each specie (indicated by the subscript ξ) per unit of volume, and it is measured in m^{-3}. In plasmas, $n_i \approx n_e$. The ionization degree α is defined as:

$$\alpha = \frac{n_i}{(n_i + n_0)}$$

where n_i is the ion density, and n_0 is the density of neutrals. In plasma physics, the kinetic energy of each specie is referred to as specie temperature T_ξ, and it is expressed in eV. A plasma is said cold if $T_e \gg T_i$.

A fundamental ability of plasma is to shield out electric potentials that are applied to it. Let us consider a charge artificially immersed in a cold plasma comprising a statistically large number of electrons and ions. Assume that the ion and electron densities are initially equal and spatially uniform. Given the higher mass and the lower kinetic energy, the ion motion can be assumed as negligible [1]. Under this conditions, the electrons will be affected by the field induced by the immersed charge. More specifically, the plasma will adjust itself in order to shield the external charge. The quantity λ_D, called the *Debye length*, is a measure of the shielding distance and it is defined by the equation below:

$$\lambda_D = \sqrt{\frac{\varepsilon_0 K T_e}{n e^2}}$$

where:

- ε_0 is the vacuum permittivity $= 8.854 \cdot 10^{-12}\ F\, m^{-1}$;
- K is the Boltzmann constant $= 1.381 \cdot 10^{-23}\ m^2\, kg\, s^{-2}\, K^{-1}$;
- T_e is the electron temperature;
- n is the ionized atom density far away (number of particles per m^3);
- e is the electron charge.

What was just presented can be better explained supposing a system of two statically charged metallic balls imposing electric field. The free charges will move to neutralize the potential. This phenomenon causes a sheath of charged particles which surrounds each samples. While moving away from the metallic surfaces, the electric potential will drop exponentially.

A criterion for an ionized gas to be a plasma is that it be dense enough that $\lambda_D \ll L$, where L is the dimension of the system. If local concentrations of charge arise or external potentials are introduced into the system, these are shielded out in a distance short compared with L, leaving the bulk of the plasma free of large electric potentials or fields. In this condition, the plasma remains quasineutral, with $n_i \approx n_e \approx n$ [1]. In addition, the collective behaviour requires

$$N_D = n\frac{4}{3}\pi\lambda_D^3 \gg 1$$

where N_D is the number of particles in a Debye sphere and with n the plasma density.

A plasma characteristic oscillating frequency is determined by the relation below:

$$\omega_p = \frac{v_{th}}{\lambda_D}$$

where v_{th} is the thermal motion velocity.
The last condition which a plasma must satisfy is:

$$\omega_p \tau > 1$$

where τ is the mean time between collisions.

1.1.1 Plasma Physics

To better understand the technology of Gaseous Plasma Antennas (GPAs), described in detail later, it is useful to investigate further the plasma behaviour. Starting from the gases, the plasma is obtained providing electromagnetic energy to the system. The knowledge of geometry, gas properties and power delivered are needed to obtain the plasma density and the temperature. In GPA the plasma is considered cold, collisional and weakly ionized [2]. A plasma is considered weakly ionized when $\alpha \leq 10^{-6}$. A plasma is said collisional when collision processes significantly affect the system dynamics.

In general, for a moving particle in an ensemble of identical or different particles with density n, the average number of collision processes in a pathlength interval Δs is given by:

$$\Delta N_c = n\sigma\Delta s$$

where σ denotes the *collision cross section*, that is schematically shown in Figure 1.1 from [3].

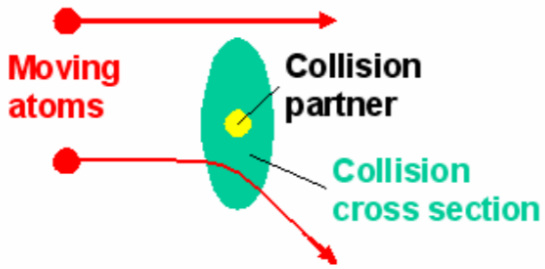

Figure 1.1: Scheme of the collision cross section (in green).

A collision cross section can be defined as the area around a particle in which the centre of another particle must be in order for a collision to occur. The *mean free path length* is the distance which is the average distance travelled by a moving particle between successive collisions. λ_c depends on the neutral density and the cross section by the relation:

$$\lambda_c = \frac{1}{n\sigma}$$

As is obvious from the last equation, to higher values of n, and σ correspond a lower value of λ_c. Hence, we can define the *collisional frequency* as the average number of collisions per unit of time in a defined system:

$$\nu_c = n\sigma v_i$$

where v_i is the particle velocity. When the power stops to flow, charged particles recombine themselves and to avoid this, electromagnetic energy is provided to accelerate electron which cause ionizations. The potential difference imposed accelerates the particles and this induces collisions. There are two fundamental phenomena which govern the plasma creation: chemical reactions and wall losses. One of the most important chemical reactions is the ionization led by collisions between charged and neutral particles. There are three types of possible collisions:

- Elastic Scattering: collision between a neutral particle and an electron thus a little loss of energy;
- Ionization: the collision between neutral and electron causing the loss of electron from the neutral;
- Excitation: the collision between neutral and electron gives to the neutral particle a discrete amount of energy (called excitation energy) that results in its alteration, from the condition of lowest energy (ground state) to one of higher energy (excited state).

The number of ionizations taking place in the unit of time is called reaction rate $K = \sigma v_i$.

For what wall losses are concerned, they are the main loss mechanism in plasmas. In a gas, a particle that hits the wall bounces back, instead in the case of plasma there is a high probability that because of the collision the wall material loses a electron or that the particle is absorbed by the wall. This phenomenon is named wall recombination and the particle have been lost. In reference to the interaction among particles and wall, the *sheath* must be introduced. One of the propriety introduced in the previous Section is the quasi-neutrality of the plasma, which is not valid near the wall. In cold plasma, the electrons have average temperature and velocity higher than ions, and near the wall more electron are lost.

As a result, close to the wall there is a charged positive area, so the plasma have a positive potential compared to the wall. Because of the potential drop, an electrostatic field is created, and this accelerates ions towards the wall and slow down electrons. So, the system tends at equilibrium creating a electric field. A consequence is the decrease of plasma density near the wall, in particular the electrons density is lower than ions one. What has just been described is important to examine the flux of particles to wall, and then the density losses. The *sheath* is based on the non-quasineutrality of plasma in that area.

The ion velocity can be obtained using the fact at the equilibrium the electron flux and ion flux must be equal; it is possible the derive the ion velocity, called *Bohm velocity*, in the sheath area:

$$v_s = \sqrt{\frac{k\,T_e}{m_i}}$$

What just introduced aim to quantify the flux of lost particles at the wall and the energy losses associated with that flux. The above losses become thermal dissipation which heats the wall.

1.1.2 Plasma Discharges

A gas discharge plasma can be defined as self-consistent state of an ionized gas as a result of passing of an electric current through it under the action of external fields. In most cases gas discharge is burnt in a cylindrical tube where a gas is located, to a given pressure, or between two parallel plates [4]. There are several natural ways to ionize particles also in standard atmosphere at room temperature; an example are the cosmic ray, which have a high energy and colliding with the atmosphere cause ionization.

The Saha equation points out the amount of ionization to be expected in a gas in thermal equilibrium:

$$\frac{n_i}{n_n} \approx 2.4 \cdot 10^{21} \frac{T^{\frac{3}{2}}}{n_i} e^{-\frac{U_i}{KT}} \tag{1.1}$$

Here n_i and n_n are, respectively, the density of ionized atoms and of neutral atoms, T is the gas temperature in $°K$, K is Boltzmann's constant, and U_i is the ionization energy of the gas expressed in ergs.

The basic elements of a gas discharge are the electrodes to which the voltage is applied, namely the cathode, and the anode. The imposed potential difference accelerates the particles from an electrode to the other, leading to the gas ionization. Since the electrodes are inside a glass vessel in our setup, the waves propagate within the plasma discharge moving energy to the particles.

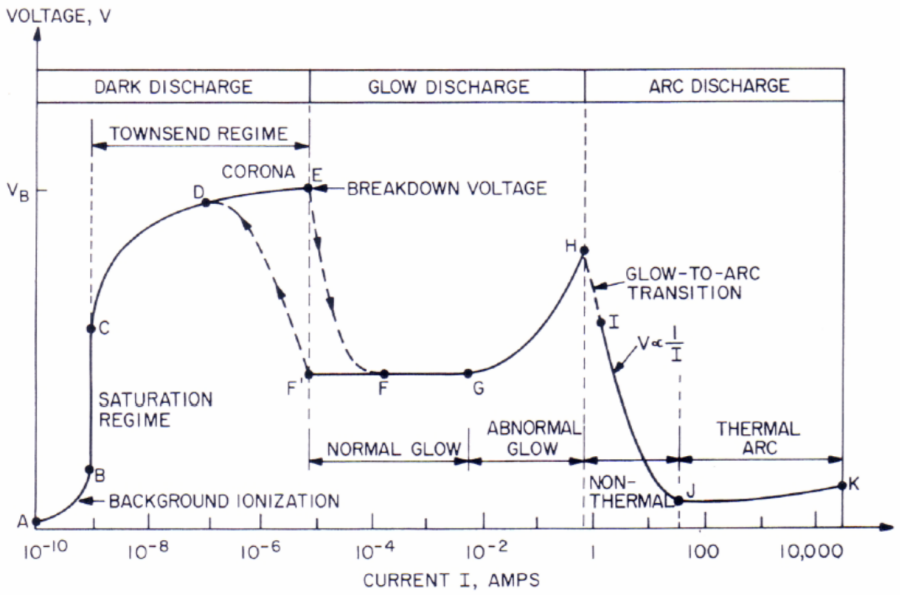

Figure 1.2: Discharge types.

The types of the plasma discharge can be various, but three main distinctions can be made, as shown in Figure 1.2:

- Dark Discharge: in this region the charge is basically in "off" mode, i.e. the discharge remains invisible to the eye. Regarding the C-E section in the Figure 1.2, the electric field is high enough so the electrons initially present in the gas can achieve enough energy before reaching the anode to ionize a neutral atom. Since the electric field becomes stronger, the secondary electron can ionize another neutral atom causing an avalanche of electron and ion. The region of exponentially increasing current is called the Townsend discharge and the process is called Townsend avalanche. In particular, acceleration of the electrons over the breakdown area is described by Townsend first ionization coefficient α. Lastly, the breakdown condition is represented by $\gamma^{\alpha d} = 1$ [5].

- Glow Discharge: this is the region of visible light, so the plasma of the discharge is luminous in contrast to the relatively low-power dark discharge. The gas glows because the electron energy and number density are high enough to generate visible light by excitation collisions. In this region, above point G, the voltage increases significantly with the increasing current in order to obtain from the cathode the desired current. As a matter of fact, the charge generation process reaches a point where the average electron leaving the cathode frees another electron.

- Electric Arc: it is a electrical discharge characterized by a very high current density and produced by an electrical breakdown of a gas. At point H, the electrodes become sufficiently hot that the cathode emits electrons thermionically. Increasing the current through two electrodes, ionization and glow discharge

can set off an arc discharge. An arc is characterized by the emission of visible light, high current density and temperature when gases are near atmospheric pressure. It is distinguished from a glow discharge because the effective temperatures of both electrons and positive ions are approximately equal. [6].

It is worthwhile to introduce two fundamental concepts, i.e. the breakdown or sparking potential (V_B) and the sustaining voltage. V_B is defined as the minimum potential difference that must be applied between cathode and anode to generate a discharge. The sustaining voltage is instead the voltage required to sustain the current flow. As is evidence from the Figure 1.2, this latter is lower than the breakdown voltage. This is because when the discharge is ignited, the plasma is more conductive than the gas, since there are more free charged particles.

For a given gas, the breakdown voltage is function of the product between the gas pressure p and the distance among the electrodes d, according to the Paschen law:

$$V_B = \frac{B\,pd}{\ln\left(\frac{A\,pd}{\ln(\frac{1}{\gamma})}\right)}$$

In the relation above, $A = \frac{\sigma_n}{kT_n}$ and $B = A\,V_i$.

In particular σ_n is the electron neutral collisional cross section, γ is the secondary electron emission coefficient, V_i is the ionization potential, T_n is the temperature of neutral atoms and, finally, $p \cdot d$ is the pressure-gap product. Examples of Paschen law as a function of pd for noble gasses are plotted in Figure 1.3.

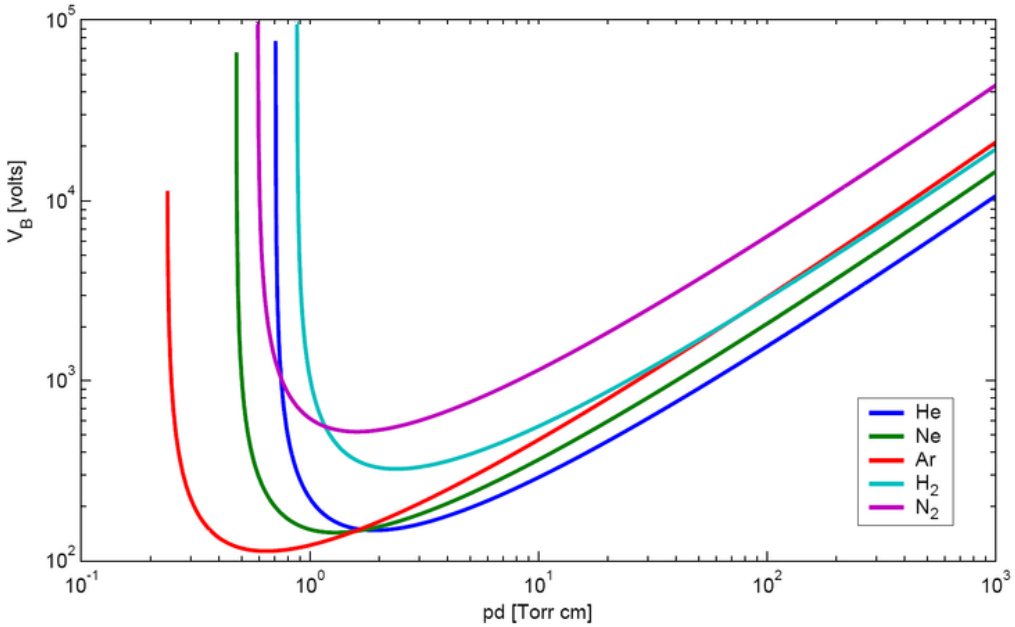

Figure 1.3: Paschen curves for different gasses.

Paschen curves are a basic instrument to study the ionization of gasses. As can be seen, they present a minimum value of voltage which corresponds to the minimum value of potential needed to generate a discharge. For values of $p \cdot d$ higher or lower than the optimum, the amplitude of the voltage to give to start the discharge, increases. Increasing the pressure, the mean free path lowers and consequentially so does the energy gained by the electrons that is not enough to guarantee the ionization. At the same time, if the pressure is lower than the optimum there is not enough number of particles to ionize the gas and the collisions with the neutral atoms are rare. Similarly, reducing the distance, under the same voltage, the electric field E is higher and the particles are more accelerated. On the contrary, if d increases, the electrical field decreases. Therefore, the breakdown voltage could be a useful parameter to evaluate if the plasma density improves or not. A numerical study has been conducted in [7] regarding the effects of V_i, γ, σ_n. It can be seen that doubling either σ_n or V_i, V_B increases for $p{\cdot}d$ on the order of hundreds $m{\cdot}mTorr$.

It is clear that the choice of the trade off between pressure and inter-electrode distance plays a fundamental role. Different factors may affect the choice of $p \cdot d$ and this causes a move away from the minimum, in the real operating conditions. Indeed, for a GPA application, even if it is important to have a low sparking potential, it is more convenient to ionize as much atoms as possible inside the vessel although the effect is a degraded power performance (i.e. an higher voltage bias). Moreover, the discharge dimensions affects the operational frequency [2], limiting the variability of the d factor.

Previous research at T4i employed various combination of length and pressure combination eventually converging on a 4 cm long cylindrical glass vessel filled with a neutral gas at a pressure of 1.5 millibar. In fact, [2] shows that if the neutral pressure increases the antenna performances (i.e. peak gain) degradate.

1.2 Antenna Overview

An antenna is an electromagnetic transducer, used to convert, in the transmitting mode, guided waves within transmission lines to radiated free-space waves, or to convert, in the receiving mode, free-space waves to guided waves [8].

Some useful parameters to evaluate the antenna performances are the input impedance, the radiation efficiency, the radiation pattern, the beamwidth, and the gain pattern. To analyse the antenna impedance, which defines the overall efficiency in terms of power transfer, a Thevenin equivalent for the antenna circuit is considered, as in Figure 1.4. The equivalent circuit includes: an ideal generator, lossless transmission line, and the antenna.

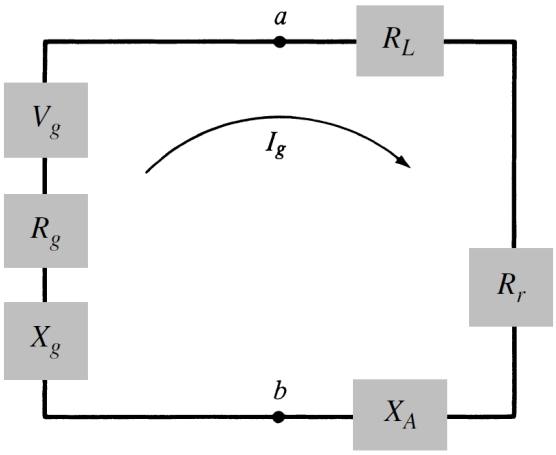

Figure 1.4: Thevenin equivalent for the antenna circuit.

Defining the input impedance as the impedance at the antenna's terminals, in the transmission mode the antenna is a passive component and is represented by a load $Z_A = (R_L + R_r) + jX_A$ connected to the transmission line. The load resistance R_L represents the conduction and dielectric losses caused by the antenna structure, while R_r is used to indicate the radiation resistance. R_r can be thought of as a resistance that, instead of dissipating power through Joule heating, emits electromagnetic waves. Also the source V_g has an internal impedance $Z_g = R_g + jX_g$.
To obtain the maximum power available at the generator delivered to the antenna, the following conditions must be met [9]:

$$R_r + R_L = R_g \qquad X_A = -X_g$$

Then, if the antenna is lossless and the conditions above are met, half of the power supplied by the generator is dissipated on Z_g, while the other half is delivered to the antenna. The antenna efficiency is defined as the ratio between the radiated power P_r to the input power P_i. From the previous relations:

$$e = \frac{P_r}{P_i} = \frac{R_r}{R_r + R_L}$$

where the antenna efficiency is defined as the ratio between the radiated power to the input one. From the previous relation, can be derived the fraction of electromagnetic power that is radiated $P_r = P_g \dfrac{R_r}{R_r + R_L}$. From this, it follows that to have an ideal $P_r \to P_g$ must have $R_L \to 0$.

Among the many graphs that describe the performances of an antenna, the Radiation Pattern is particularly important, and can be considered to be representative of the relative field strengths of the field radiated by the antenna [10]. The radiation pattern can be defined as a mathematical function or a diagram representing the radiation properties of the antenna as a function of space coordinates, as shown in the Figure 1.6 from [9].

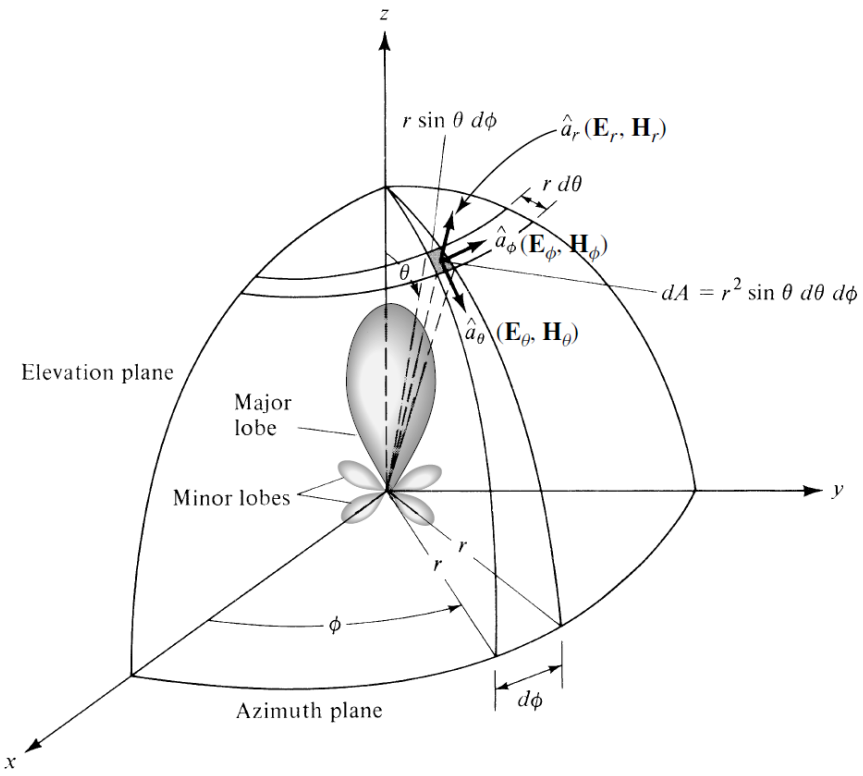

Figure 1.5: Coordinate system.

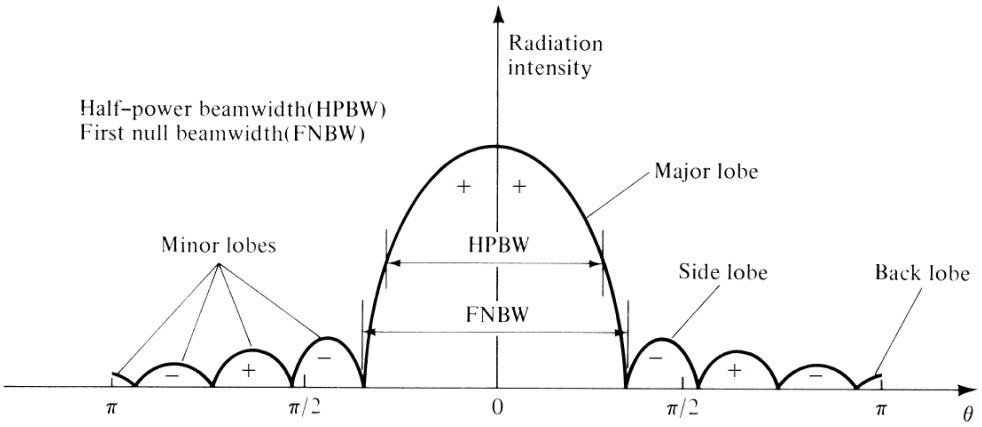

Figure 1.6: 2D Radiation pattern.

The graph correlates the value of a physical quantity, like power flux, radiation intensity, directivity, field strength, calculated on a surface with constant radius with respect to the observer's position, with the angular coordinates θ and ϕ as shown in Figure 1.5. The radiation pattern can be drawn both in 2D, 3D or polar coordinates, depending on the requirements and needs. Parts of the radiation pattern are called *lobes*, which may be classified into a major, side, and back lobes.

A major lobe, also called the main beam, is defined as “the radiation lobe containing the direction of maximum radiation” [8]. Therefore it appears that a side and the back lobe represents radiation in undesired directions, so they should be minimized. Hence, no antenna is able to radiate all the energy in one preferred direction, and some of that is radiated in other directions with lower levels than the main beam. Classifying an antenna based on the shape of the plot we have the following definitions. An isotropic antenna is a lossless ideal antenna which has equal radiation in all direction. On the contrary, an antenna is defined directional, i.e. reflector antenna, if efficiently radiates or receives electromagnetic waves in some directions. Ultimately, a omnidirectional antenna, like a dipole, radiates electromagnetic waves in all directions on a plane with uniform power.

A basic parameter associated with the pattern is the Beamwidth, defined as the angle for which the antenna radiates with maximum power. It is calculated relative to the major lobe which identifies the main direction. It is commonly referred to the Half-Power Beamwidth (HPBW) define by IEEE as "In a plane containing the direction of the maximum of a beam, the angle between the two directions in which the radiation intensity is one-half value of the beam” [9].

Another important parameter that can be easily estimated from the radiation pattern of the antenna is the Directivity, can be defined as the portion of power in a generic direction with respect to the radiation intensity averaged in all directions:

$$D = \frac{U}{U_0} = \frac{4\pi U}{P_{rad}}$$

where:

- D= Directivity
- U= radiation intensity (W/unit solid angle)
- U_0 = radiation intensity of isotropic source (W/unit solid angle)
- P_{rad} = total radiated power (W)

The antenna gain is a parameter that takes into account the directional capabilities of antenna, as well as its efficiency:

$$G = e\ D$$

1.3 Gaseous Plasma Antennas

1.3.1 Overview

GPAs are devices that rely on a partially or fully ionized gas to radiate EM waves, thus differing from the traditional antenna design that is based on metallic wires and/or surfaces. Though the idea is not new [11], only recently the feasibility has been demonstrated [12]. GPAs consist of a dielectric vessel filled with some neutral gas such as argon that is energized by any generation method to form a plasma. A metal circuit, here in after referred to as signal coupler, is wrapped around the tube or in contact with the plasma itself to inject the signal frequency into the plasma. In a GPA, the plasma is actually powered by two different frequencies simultaneously: a generation frequency to drive the plasma discharge and a working frequency to apply the signal so that it might be used for either transmission (both frequencies switched on) or reception (only the driving frequency switched on) [13]. The operation of a plasma antenna depends upon the interaction of EM waves with the plasma [14], and relies on the property of plasma to behave frequency-dependently when an EM wave impinges on a plasma volume. If the EM wave has frequency higher then the plasma frequency, it passes through the plasma without attenuation. On the contrary, if the incident EM wave frequency is lower than the plasma frequency, the plasma behaves as a metal conductor. Thanks to this property, a plasma column can be used to radiate EM waves with frequency below the plasma frequency but offering more degrees of freedom than metallic antennas [15]. When the plasma is on, GPAs might offer several advantages, namely:

- they are transparent to incoming EM waves whose frequency is greater than the plasma frequency, thus reducing interferences;
- they can be reconfigured with respect to frequency, gain and beam-width;
- they are reconfigurable electrically rather than mechanically on time scales of the order of microseconds to milliseconds;
- they can be stacked to form arrays, as GPAs operating at different frequencies do not interfere with each other.

When the plasma is off, the GPA reverts to a dielectric tube with a very low radar cross section, and such a feature makes GPAs appropriate for stealth communications; co-site interference and/or parasitic interference can be greatly reduced using plasma antennas because GPAs not in use can be turned off in micro to milliseconds with the plasma being extinguished. These features make GPAs very promising for space communication, where electric reconfigurability, and the possibility to stack several antenna in a small environment without interfering with each other can be very convenient.

In spite of the fascinating advantages of plasma antennas with respect to their metallic counterparts, plasma discharges used in communication systems may introduce some issues, as their complexity. Specific attention must be paid to the noise introduced by the plasma, the complexity of the plasma antenna, and the availability of suitable technological solutions to generate the plasma. However, thanks to the introduction of Radio Frequency (RF) generation method and the employment of pulsing power technique, is possible to obtain lower noise levels, higher plasma density and reduced power consumption [16].

In GPA applications, the plasma is cold, weakly ionized, and unmagnetized [17]. In these conditions, the plasma can be represented by the Cold Fluid Model. According to this model, the plasma permittivity yields:

$$\epsilon_r = \frac{\epsilon}{\epsilon_0} = (1 - \frac{\omega_{pe}^2}{\omega^2 + \nu^2}) - j\frac{\nu}{\omega}(\frac{\omega_p^2}{\omega^2 + \nu^2})$$

where ϵ is the material permittivity, ϵ_0 is the vacuum permittivity, ω is the working frequency, ω_{pe} is the electron plasma frequency defined as:

$$\omega_{pe} = (\frac{n_e q_e^2}{\epsilon_0 m_e})^{\frac{1}{2}}$$

ν is the electron-neutral collision frequency and j is the imaginary constant.

1.3.2 The Gaseous Plasma Dipole

A gaseous plasma dipole is comprised of two cylindrical and collinear plasma discharges in an arrangement that resembles that of a conventional metallic dipole. In [2] a gaseous plasma dipole working in the range 0.3 - 3 GHz was considered to study the physics of operation of a GPA and to analyse the influence of plasma parameters in the antenna performance. In [2] the signal injection was achieved by means of two plate electrodes placed at the inner edges of each discharge.
Full model description can be found in [2].

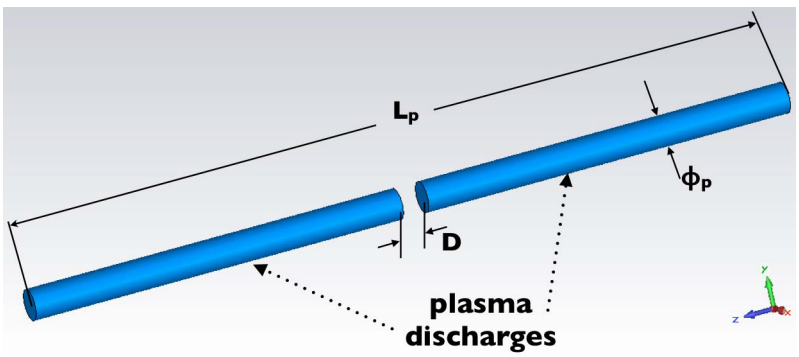

Figure 1.7: Model of the plasma dipole.

During antenna operations, the antenna angular frequency is strictly less than the electron plasma frequency; consequently, the cylindrical plasma column behaves as an open waveguide that can sustain surface-wave propagation and that radiates significantly. The surface wave on the plasma column has a shorter wavelength than would have on a metallic column and it is weakly damped in the whole range of frequencies. The two open ends represent discontinuities with a unit reflection coefficient; in such a cavity, a standing wave develops. For very low frequencies, the plasma column behaves as a conventional metallic dipole would do, with a strongly capacitive impedance. As the frequency increases toward the first resonance (*short-circuit resonance*), the dispersion properties of the plasma occur. The plasma column in the UHF frequency band shows an effective wavelength which is shorter than the free space wavelength. This ultimately leads to a downshift of the resonant frequency with respect to what expected for a conventional metal dipole. For a comprehensive mathematical description, see [2].

In Figure 1.8 from [2] is shown the radiation pattern of the plasma dipole at the short-circuit resonance frequencies, and this last resembles that of an ordinary perfect electrical conducting (PEC) dipole.

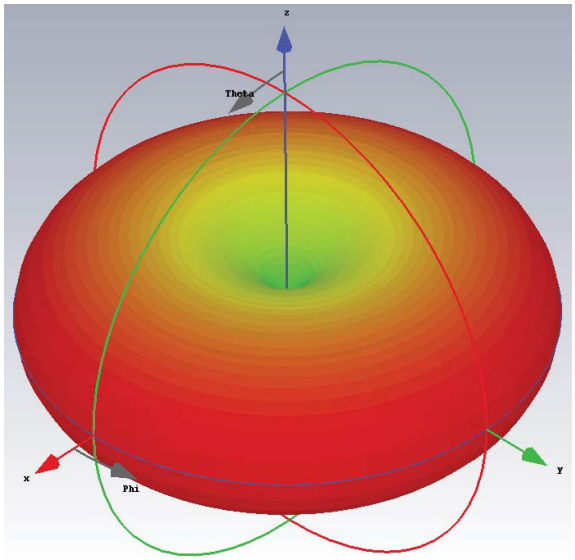

Figure 1.8: Gain pattern of finite-length plasma column at the first short-circuit resonance frequencies.

If the length of the plasma column is reduced, the resonant frequency rises, similar to the case of a conventional RF dipole. In [2], the effect of the plasma density on the antenna performances was studied. The first short-circuit resonance frequency decreases as the density does; similarly, the radiation efficiency decreases (the losses become higher as the plasma density decreases), whereas the gain pattern remains the same. In other words, the resonance frequency of the GPA can be tuned by varying the plasma density therein [2].

In [2] it was also considered the role of other parameters, like the type and the pressure of the neutral gas, that are relevant to the generation of the discharge. In fact, different gasses have different ionization energies, which result in different amounts of power needed to generate the plasma. Considering only monoatomic gas species, the only effect of the different gas atoms, as the gas species varies, is to slightly change the electron-neutral collision frequency. Anyway, the gain pattern resembles that of a PEC dipole independently of the type of gas. As regards the neutral gas pressure, if this last increases, the electron-neutral collision frequency does so. It can be proved that the effect of the neutral gas pressure on the resonance frequency is negligible [2]. The antenna gain patterns at resonance maintain the shape that a PEC dipole would have, independently of the gas pressure; however, the antenna peak gain value attains remarkably lower values as the neutral pressure is increased. This behaviour can be motivated by the increase of the electron collision frequency, and this, in turn, leads to higher losses within the plasma discharge and, consequently, a decrease of the gain.

The introduction of a magneto-static field was also investigated, since it could help confine the plasma, and thus reduce the losses in a low pressure discharge, and ultimately make the plasma generation more efficient. However, the introduction of a magneto-static field makes the plasma anisotropic, which affects the propagation phenomena on the plasma column, and ultimately the antenna performance. Moreover, the presence of any conductive or ferromagnetic material near the dipole increases the complexity of the plasma dipole setup and could change the antenna performance by perturbing the boundary conditions that the fields radiated by the dipole must satisfy. The magnetostatic field has a negligible effect on the gain and on the radiation efficiency. As the magneto-static field increases, the first short-circuit resonance frequency shifts up and the peak gain increases weakly, while the gain pattern keeps unchanged.

1.3.3 Cold Cathode Fluorescent Lamp

To implement practically a gaseous plasma dipole into a prototype, plasma sources resorting on Cold Cathode Fluorescent Lamps (CCFL) can be used. A CCFL is composed of a glass cylindrical vessel filled with a Penning gas mixture of noble gases or nitrogen and a small addition of mercury. The electrical connection is established by means of two electrodes placed at both ends of the tube. The Paschen's law is the basis of the lamps work, in particular, the CCFLs follow the principle governing the glow discharge (see Figure 1.2).

To the electrodes is applied high voltage (on the order of 150 V in normal operations) at high frequency (around 20 kHz) and this causes the decomposition of the gas leading to the formation of a plasma. The energy emitted by the excitation of mercury in the UV band is then absorbed by a uniform coating of phosphor which, in turn, radiates visible light [5]. Due to the timely and readily availability of CCFL lamps on the market, most of the preliminary work on plasma antenna was per-

formed using such devices. However, commercially available CCFLs are limited in shapes and dimensions. Moreover, no knowledge neither control on the gas pressures and mixtures can be inferred, thus preventing a proper analysis and development of a GPA. Thus, the research is moving onto custom-designed vessels, in order to have control over length, shape, gas mixture, enclosure film choice and electrode design. We have to point out, however, that CCFL lamp technology maximizes luminosity over any other factor, but for our purposes, the electron density is much more important.

1.4 Prototypes under development

A gaseous plasma dipole working in the range 0.5 - 1 GHz is currently under development in T4i, with University of Padova. The prototype is comprised of 2 glass vessels filled with argon at a pressure ranging between 1 and 2 mbar. To ignite the plasma and sustain the discharge, RF power is applied to commercial Cold Cathode Fluorescent Lamps (CCFL) electrodes soldered to the glass and in contact with the plasma itself. The inner CCFL electrodes are used also for the injection of the signal. In Figure 1.9 a) is shown a CAD model of a generic vessel and it may be noted that the main two components of any vessel are the two electrodes and the glass. In Figure 1.9 b) from [18] are presented tipically values of the vessel dimensions.

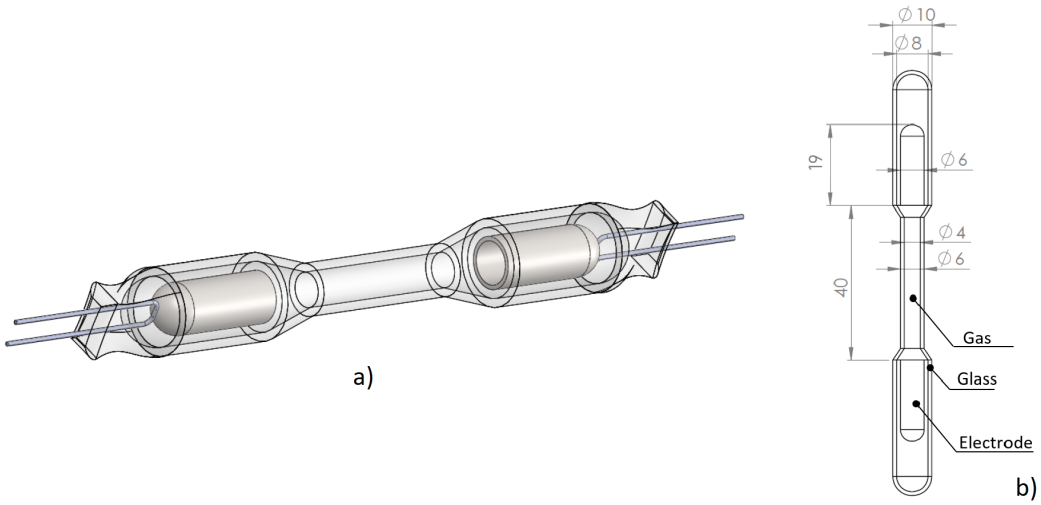

Figure 1.9: CAD model for a generic vessel.

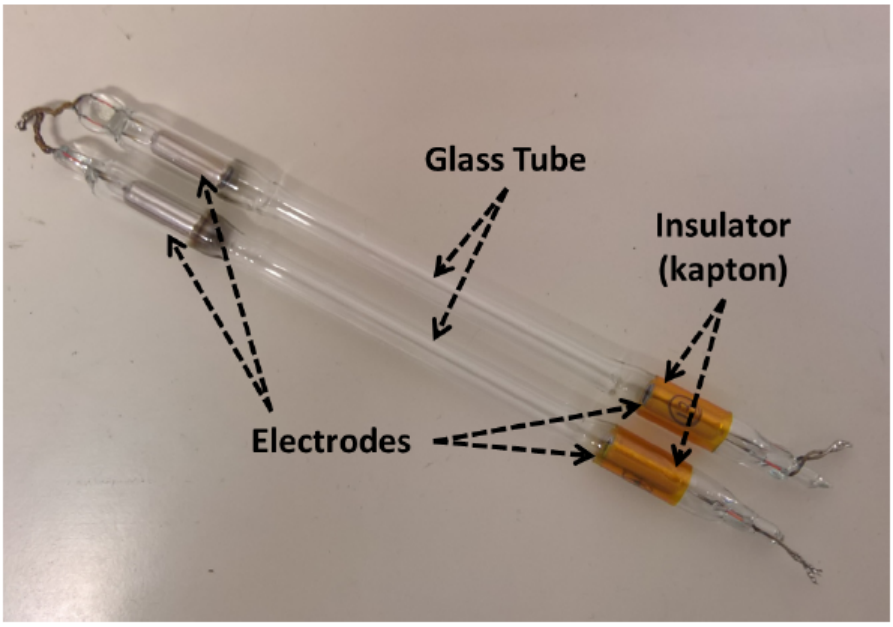

Figure 1.10: Picture of two plasma element connected in series.

Depending on the size of either of them, different versions of CCFL-GPAs have been developed. That CAD model should be considered as a module used in conjunction with other elements to form a radiating element. The length of the vessel is calculated as inter-electrode distance and it can vary between a minimum of 34 mm and a maximum of 100 mm. The different lengths depend on the setup which they are designed for and so on their purpose.

The vessel section is irregular to accommodate the shells, while the residual flattening at the ends is a consequence of the manufacturing process. Hence, the overall length of the vessel might change, but even so, the electrode portion of the vessel is fixed. The external glass casing is a hollow structure 1 mm thick throughout the whole vessel, except at the ends, where the glass is fused. The enclosure by itself weighs less than 10 grams.

The shell is a CCFL-compliant electrode, characterized by a hollow cylindrical structure with a semispherical cap 0.5 mm thick, with a wire bent and soldered to the metal. There are two ends of the same wire how can be seen in Figure 1.11, and this is useful to create less cluttered connections.

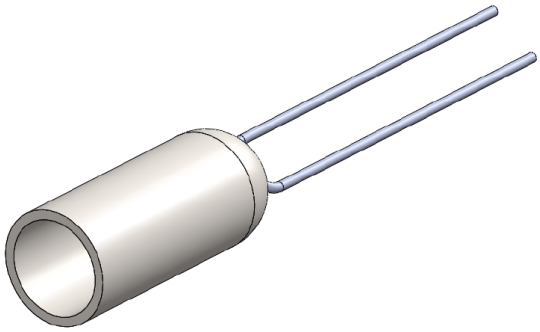

Figure 1.11: CAD model for a generic shell.

In this work will be considered a length vessel of 50 mm and diameter of 4mm. In Figure 1.11 is presented a CAD model of the electrode, where it possible to understand better its hollow structure and shape. Early designs involved the use of commercial CCFL lamps, used as proof of concept.

CHAPTER 2

Research

2.1 Problem Statement

It was shown that increasing the plasma density results in an enhancement of the antenna gain [2]. In this study, the use of different materials to increase the plasma density, and consequentially the antenna gain, was investigated. Until now the external casing of the plasma source, as shown in Figure 1.9, was considered made of glass (i.e. soda lime). Although, to improve the electron density value of a GPA in the same working conditions, it has been thought to replace or coat the glass with a material which presents a high value of Secondary Electron Emission Yield (SEEY). Secondary electron emission processes, under electron bombardment, play a fundamental role in the performance of a variety of electron devices. Indeed, this phenomenon involves different applications, and in literature is possible to find references to it in articles concerning Plasma display, Fluorescent lamps, Micro channel plate detectors, Hall thrusters. The materials used in the devices may need to be judiciously selected in some cases to enhance the secondary electron emission and in other cases to suppress it. It is anticipated that the selection of the materials concerns the insulating category, in particular ceramic oxide. This is because, in that latter, the wide band-gap prevents low energy secondary electrons from losing energy through electron-electron collisions, thereby resulting in a large escape depth for the secondary electrons and a large secondary electron yield. In general, insulating materials have high secondary electron yields, but a provision to supply some level of electrical conductivity is necessary in order to replenish the electrons lost in the secondary-electron emission process [19]. In this Chapter the research about materials with enhanced SEEY is presented, starting by reporting the theoretical overview of the fundamental phenomena from which is obtained the secondary electron emission yield. Then, the following Section includes the investigation in literature of the materials that present the features searched for

the aim; so in conclusion is shown the most convenient choice, as combination of availability, costs and material properties.

2.2 Material selection process

2.2.1 Secondary Electron Emission

Secondary emission processes involves several factors and phenomena. Due to the complexity of the phenomenon, there are several theoretical and numerical models which have been developed. They were able to predict most of the important characteristics of secondary electron emission. To mention a few, the secondary electron yield as a function of primary electron energy [20] and the energy distribution of the secondary electrons [21].

Secondary electron emission processes can be divided into three fundamental steps, namely (i) the penetration of the primary electrons, (ii) the transport of the internal secondary electron to the surface, and (iii) the escape process of the secondary electron at the material interface. For what the penetration of the primary electrons is concerned, the primary electrons are assumed to travel in a straight-ahead path, slowing down due to collisions with electrons and ions and transferring kinetic energy, and so generating secondary electrons. According to [21] [22], *N(x)* is defined as the number of secondary electrons produced in the layer *dx*. It is assumed to be equal to the energy loss in the layer *dE* divided by the average excitation energy *B*. The final relation is obtained (see [22] for more detail):

$$N(x) = \left(\frac{A}{2}\right)^{\frac{1}{n+1}} \frac{1}{B(R-x)^{\frac{n}{n+1}}} \tag{2.1}$$

where A is an arbitrary constant, B is the excitation energy and the maximum penetration depth is:

$$R = \frac{E_o^{n+1}}{(n+1)A}$$

where E_o is the initial energy of the primary electrons and A is an arbitrary constant. By electron transmission measurements in Al_2O_3, n was estimated as 0.35 in [23]. From 2.1 it is clear that is important increasing secondary electron production near the end of the primary-electron path. In addition, analysing the definition of R it can be concluded that the penetration depth of the primary electrons increases with increasing energy. Another phenomenon to be taken into account for the penetration of the primary electrons is the elastic backscattering, i.e. the secondary electrons retain their energy and reverse directions, escaping through their original trajectories. Therefore, the yield from elastic backscattering is defined as the ratio of the secondary electron flux which is elastically backscattered to the flux of primaries [24].

The transport of secondary electrons through the material is modelled by either a single-scattering process or by a diffusion process which involves a large number of scattering events. In general, if a primary electron has energy high enough, it generates many internal secondary electrons. The secondary electrons lose energy through the excitation of valence electrons into the conduction band [19]. The energy-loss mechanisms for internal secondary electrons depend on the material. In the case of insulators, the minimum kinetic energy for a secondary electron to escape called *electron affinity* χ, which is typically on the order of an electron volt.

Thus, the last step which characterizes the phenomenon is the escape process of secondary electrons at the solid-vacuum interface[19].
The SEEY is defined as the ratio between the secondary electrons which escape at the solid-vacuum interface and the primary electron flux which hits the surface. However, in literature, there are variations in measurement technique and definition of SEEY [25]. To calculate the SEEY, several set-ups have been developed. Therefore its value, for a certain material, may vary depending on the implemented set-up, assumptions made, as well as the sample preparation and handling, the tilt angle of the ion beam which impacts the specimen, the measurement procedures, the numerical model to which is referred to. For example, in the work shown in [26] [27] a cleavage tube with an internal coating of tin oxide as an electron collector has been used. The primary pulse was measured with the help of a suppressor grid negatively biased relative to the target, while the secondary current was measured with the grid positively biased with respect to the target. The SEEY is taken as the ratio of the secondary pulse to primary pulse measured. A similar setup was adopted in [28] for the measurement of secondary electron emission from organic compounds. With the use of electron pulsing and a hemispherical electron collector, SEEY is defined as the ratio between collector current to the sum of target and collector currents. It is difficult to observe high secondary electron yields because most of the internal secondary electrons lose sufficient energy through collisions with electrons and ions to fall below the vacuum level.

However, it should be pointed out that, when the secondary electron yield coefficient exceeds one, the number of emitted secondary electrons is higher than the number of arriving primary electrons. This work aims to increase the plasma density, so it would be convenient to have the SEEY as high as possible. So, it is possible to quantify the secondary electron emission through the SEEY. An example of set-up is shown in Figure 2.1 from [25].

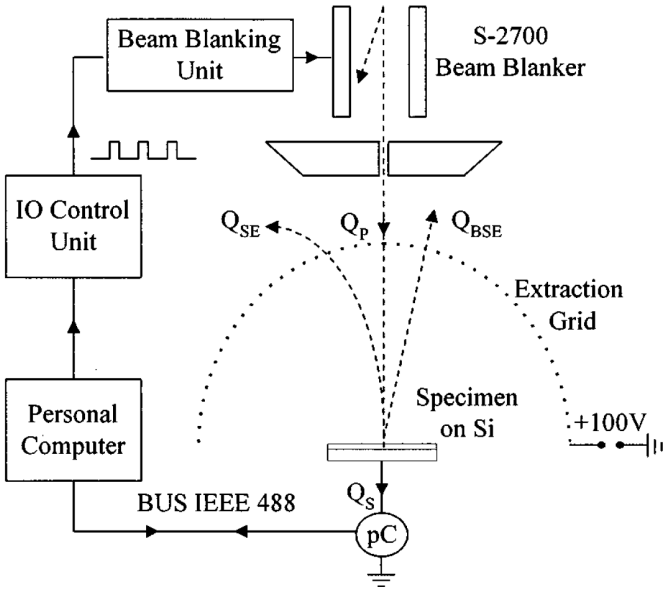

Figure 2.1: Example of set-up to quantify the SEEY.

According to [29] [19] SEEY is determined by measuring the specimen current after biasing the specimen in two separate experiments. In the first measurement, the specimen is positively biased in the effort to force all emitted secondary electrons to return to the surface. Subsequently, the specimen is biased at a negative voltage to repel all secondary electrons from the surface. The difference in specimen current measured under the different states is taken as the secondary electron emission. Consider now a situation where the insulating film is irradiated with a single electron dose. If the total electron emission from the insulator is above the primary electron dosage, a positive surface charge will be generated. Conversely, negative charging occurs with a net accumulation of electrons on the sample when the total electron emission is less than the primary electron dosage [25]. Hence electron charge Q_s will be induced in the substrate as defined by

$$|Q_s| = |Q_T| - |Q_p| \qquad positive\ charging$$

$$|Q_s| = |Q_p| - |Q_T| \qquad negative\ charging$$

where Q_p and Q_T are the primary electron charge injected and total electron charge emitted, respectively. Accordingly, it is possible to find out the total charge emitted. The SEEY can be calculated in the following way:

$$\delta = \frac{Q_T - Q_{SBE}}{Q_p}$$

where Q_{BSE} is the backscattered electron charge and $Q_T - Q_{BSE}$ is the secondary electron charge. Point out that the contribution of backscattered electrons may become more significant at large surface tilt [25].

Taking said considerations into account, in the next Section will be presented the materials research based mainly on the SEEY, relying on the value and the trend to varying of electron volt (eV) which are presented. The energy owned by the charged particle flux which hit the material is another parameter that contributes to the SEEY. Unfortunately, it is not possible to quantify the energy flux at the walls in our sources, but in previous report [30] the electron temperature was estimated as $T_e < 10\ eV$. This will support the research and the selection of the possible materials to improve the plasma density.

2.2.2 Materials Research

As discussed above, the working principles of the plasma source for GPA applications and CCFL are based on the same mechanism. Obviously, the aim of the two devices is much different. The GPAs, indeed, take advantage of plasma to transmit signals, the lamps to release light radiation. Since the sources here presented for GPA applications and CCFLs share the same commercial electrodes and plasma generation mechanism, the lamps are a great starting point for the materials research.

For the improvement of the lamps performances, one of the most mentioned materials is Magnesium Oxide (MgO). Referring to lamps, the figures of merit are parameters related to the emitted light, i.e. luminance and luminous efficiency. In spite of the parameter are different, the secondary electron emission is taken into account. Several tests were carried out to verify if the addition of this material brought benefits in terms of performance. In some cases MgO is added on the phosphors in the form of nano-crystal, or a thin film of MgO is deposited by e-beam evaporation on the dielectric material [31]. Moreover, MgO is used as a coating on the electrodes [32]. In the latter case, the MgO coating allows the reduction of the lamp voltage and the ignition voltage, the increasing of luminance and luminance efficiency, and the reduction of generated heat. It was verified in [33] that also the coating on the dielectric material produces good results .

There is a strong correlation between the sparking voltage and the secondary electron emission yield of the dielectric materials by ion bombardment. In the case of the Plasma Display Panels, the sparking voltage decreases when the dielectric material has high yield [33]. In [33] it was obtained that MgO and La_2O_3 are the most suitable panel material for the present case. Above all the panel with a protecting layer of MgO shows not only decreased sparking voltage but also considerably improved operating stability and lifetime. The SEEY is strongly dependent on the electron affinity of the dielectric material. As it is shown in [33], the electron affinity of MgO is 0.6 eV, whereas for La_2O_3 is 0.67eV, so the consequence is that the MgO has a SEEY higher than La_2O_3.

It is possible to enhance the MgO behaviour by adding titanium oxide (TiO_2) [34]. $Mg_{2-2x}Ti_xO_2$ films were prepared by an e-beam evaporation method to be used as possible substitutes for the most usual MgO coatings. In [34] it has been noted that when the $\frac{TiO_2}{MgO+TiO_2}$ ratio is equal to 0.1 and 0.15, the deposited films exhibited the secondary electron emission yields improved by 50% compared to that of the conventional MgO. But it is necessary to consider that the addition of TiO_2 to MgO involves little compressive stress. It is apparently expected from the fact that the ionic radii of Ti and O are larger than that of Mg. Furthermore, depending on the ratio the surface roughness changes, indeed if the ratio is equal to 0.1 the roughness is lower. The roughness problem will be briefly discussed later, together with the coating thickness and the tilt angle of the particles that hit the vessel. These parameters affect the secondary emission. However a detailed study about them is not the main purpose of this study.

Microchannel plate detectors are another technology which takes advantage of the SEE phenomenon. A microchannel plate detector consists of a glass track which includes hundreds or thousands channels. The inside of each channel is coated with a material that produces secondary electrons. In this framework, several materials have been studied, multilayered $MgO-TiO_2$ included. Indeed in [35] the following samples to compare have been prepared: monolayer MgO, monolayer MgO with a monolayer of TiO_2 over the surface, alternating layers of MgO and TiO_2, monolayer TiO_2. Firstly, it was noted that even minor changes in the surface composition strongly affect the secondary electron emission properties of materials. Secondly, it was verified in [35] that the $MgO-TiO_2$ combination coating has a better behaviour compared to a mono-material coating. For a layered $MgO-TiO_2$ structure (a monolayer of $TiO2$ on top of MgO film), it was observed that Ar^+ sputtering resulted in a larger SEEY increase with respect to the other samples. What happens is that after ion sputtering some Ti was mixed within a few top-most layers of MgO, thus allowing it to act more as a dopant rather than an interface. Whereas in the alternating layer of MgO and TiO_2, the TiO_2 monolayers are untouched and intact so that the top-most layer became a doping layer while the lower layers remained to hinder the emission of secondary electrons created deeper within the sample.

A further remarkable material might be the Al_2O_3. In literature there are various comparisons between Al_2O_3 and MgO (as in the report [35]), for this reason, it was considered worthwhile to deepen the study. As already said, one of the technologies where the secondary emission is studied is the Hall thrusters. Many comparisons among different materials have been made, especially borosil ($BN-SiO_2$), alumina Al_2O_3, silicon carbon (SiC), graphite [36]. The results of the comparison studied in [36] are shown in Figure 2.2. It must be pointed out that the diagram shows $\delta+\eta_r+\eta_i$ that is the total secondary electron emission yields, where δ is the true SEE yield, η_r is the elastic reflection yield and η_i is the inelastic backscattering yield.

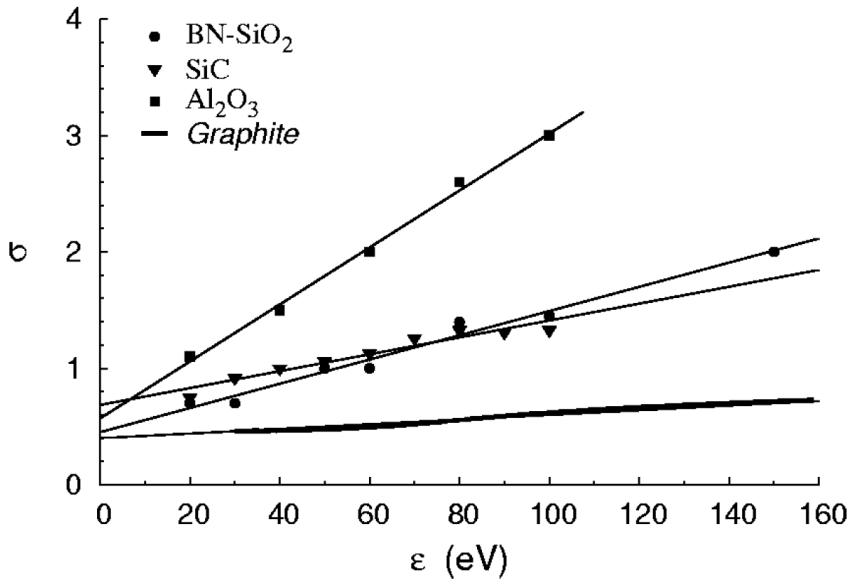

Figure 2.2: Total SEEY $\delta + \eta_r + \eta_i$, where δ is the true SEEY, η_r is the elastic reflection yield, and η_i is the inelastic backscattering yield, experimentally obtained in [36] as a function of the primary electron energy.

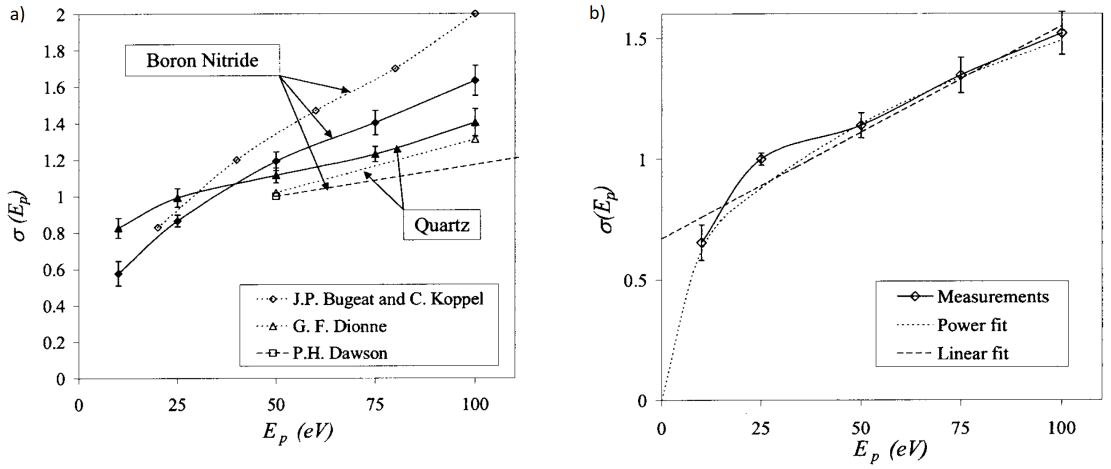

Figure 2.3: Total SEEY $\sigma = \delta + \rho$ of a) boron nitride, quartz and b) macor, where δ is the true SEEY, ρ is the coefficient of backscattering, experimentally obtained in [37] as a function of the primary electron energy.

As can be seen in Figure 2.2 from [36],the materials with a higher yield at energy lower than 20 eV are Al_2O_3 e SiC. Figure 2.3 shows the results obtained in [37] for the total SEEY of boron nitride (BN), quartz (SiO_2), macor (made up of fluorphlogopite mica in a borosilicate glass matrix) as a function of the primary electron energy. It is noteworthy that in this case $\sigma = \delta + \rho$ represents the total yield of

secondary electron emission, so the coefficient of backscattering ρ is taken into account. In the figure above the results are also presented as a comparison between experiment and the mathematical model used, and will not be examined.
In [38] it was shown that incorporating Caesium in the MgO thin films improves the SEEY. The SEEY is affected by the work function of the material, i.e. is the minimum energy needed to remove an electron from a solid. So, a low work function material is very useful for improving the secondary electron emission yield. Caesium has a very low work function value, 2 eV, and the value is much lowered when caesium oxide is formed at the thin film surface. Caesium incorporated MgO thin films show the same crystalline structure as the evaporated MgO and is an effective method for improving the secondary emission yield, as can be seen from the results shown in [38].

Thickness, Roughness and Tilt Angle

The SEEY is affected by many factors, including the coating thickness, the surface morphology of the coating and the tilt angle of the particles that hit the sample surface. In literature, there are many works about tests to understand how the SEEY is affected by these three parameters.

As regards the thickness, the SEEY behaviour as a function of thickness for magnesium oxide has been investigated in [39]. Two series of MgO thin films having various thicknesses were prepared on a Si substrate by electron-beam evaporation and by spin coating of MgO precursor solutions. It was verified that the magnitude of the secondary electron emission yield of the MgO layers strongly depends on the film thickness. For the tests procedure see [39]. The maximum SEEY of the each MgO film on the Si substrate was observed when the penetration depth of primary electrons was close to the thickness of the coating if the applied electric potential to the sample was about 45 V. On the other hand, under a strong electric potential (i.e. around 1000 V), an extra thickness of MgO film is allowed to supply electrons by electron tunnelling mechanism. There is indeed a dependence among the SEEY and the sample bias voltage. Note that different materials have distinct escape depths of secondary electrons, and this must be taken into account whene selecting the material and the deposition thickness.

In figure 2.4 from [25] is shown the trend of the normalized SEEY as a function of the tilt angle of the particles beam that hits the specimen made of quartz (SiO_2). It is evident that the higher the tilt angle, the higher the normalized SEEY. For what the roughness is concerned, it has been tested in [40] that the increase of secondary electron yield for conducting materials due to the introduction of surface roughness. In general, rough surfaces present tilted microscopic surfaces to the incident beam and result in higher secondary electron emission.

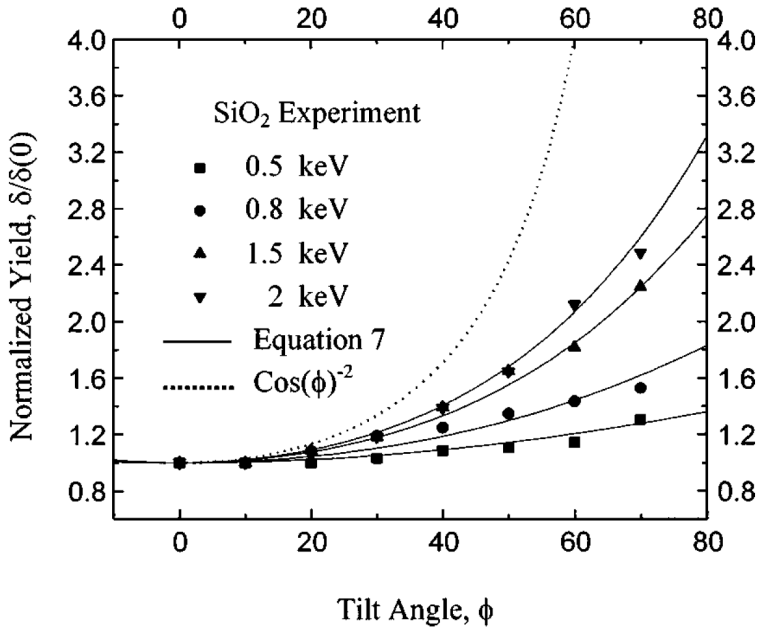

Figure 2.4: The normalized SEEY $\delta/\delta(0)$ for SiO_2 experimentally obtained in [25] as a function of the tilt angle ϕ of the particles beam that hits the sample. The result is reported for different primary electron energy according to the equation $\frac{\delta(\phi)}{\delta(0)} = e^{k[1-cos(\phi)]}$ and $cos(\phi)^{-2}$.

2.2.3 Materials Analysis Conclusions

It is worth to be noticed that one of the main purpose of the present work is to obtain a competitive device in terms of both performances and cost. In this effort, the cost of the raw material, and of the manufacturing was also considered as a driver parameter in the material choice.

According to what found in literature and on the best compromise between the material availability and cost and the secondary emission properties, the following choices have been made:

- Magnesium Oxide (MgO)
- Titania (TiO_2)
- $MgO - TiO_2$
- Boron Nitride (BN)
- Alumina (Al_2O_3)
- Quartz (SiO_2)

An option which has been considered is to totally substitute the glass for the confining vessels. However, the electrodes commercially available are encased in soda-lime glass. Thus, the only part of the vessel that could be successfully substituted is the cylindrical part (see Figure 1.9) onto which the glass enclosing the electrodes would be soldered. To this purpose, Al_2O_3 and SiO_2 have been selected, given that cylindrical tubes of the desired dimension (i.e. inner diameter of 4 mm) are available on the market. Unfortunately alumina and quartz are not compatible with the glass to which the electrodes are soldered, and the welding between them was not successful.

For these reasons, it has been opted for the deposition of MgO, Al_2O_3 and TiO_2 layers on the glass by means of the *Sol-Gel method*. This process has been chosen because it allows to obtain the required coating in a rather fast, monitored and cheap way. Moreover, the sol-gel method is a low-temperature technique (i.e. 500 °C), so the heat treatment temperature is lower than the softening temperature of the glass (i.e. 700 °C). All the steps for the coating implementation will be shown in the following Chapter. As regards to the boron nitride, BN-based sprays are available on the market. The BN was sprayed inside the glass cylinder. Such material in this form must be allowed to dry for a few hours.

CHAPTER 3

Coatings deposition

3.1 Introduction

As mentioned in the previous Chapter, it was decided to realize the coating of magnesium oxide, alumina and titania on the glass substratum. The method to make a thin film used in the present work is named *Sol-Gel*. The reason of this choice is because the sol-gel method allows to obtain the required coating in a rather fast and cheap way. In this Chapter the all procedures carried out to realize the films will be described. Moreover, it will be shown how the various steps have been improved and optimized. This method represents one of the techniques most studied and employed to obtain high quality ceramic materials [41], [42], [43]. Despite this, there are no examples about the use of this method in the current application, so it will needed to verify that it is suitable for the aim of this study. It is important to highlight that the choice of a method rather than the other could affect the material yield in the working condition. This part of experiments was performed at laboratory of University of Padova, since chemical processes are involved.

3.2 Sol-Gel Method

The sol-gel process is a widespread method to obtain vitreous and ceramic materials. The process involves conversion of monomers into a colloidal solution (sol) that acts as the precursor for an integrated network (or gel) of either discrete particles or polymers. A sol is a stable suspension of colloidal solid particles within a liquid. A colloidal system is a mixture where a matter is microscopically dispersed. Instead, a gel is an porous 3-dimensionally interconnected solid system which expands in a stable fashion throughout a liquid medium. The nature of gels depends on the

coexistence between the solid and the liquid medium. At this point, the next process introduced is the gelation. A gel takes form when the homogenous dispersion present in the initial sol rigidifies. The gelation prevents the development of inhomogeneities within the material. At the gel-point the sol sharply changes from a viscous liquid state to a solid phase called the gel [42].

This approach is a cheap and low-temperature technique that allows the fine control of the product chemical composition. It can be also simply applied to materials such as glass, metals and ceramic. The interest is encouraged by the extreme versatility of this method, and it has many advantages compared to the traditional techniques because this process can be easily monitored. The sol-gel method allows the production of new hybrid organic-inorganic materials which do not exist in nature. Moreover, the chemical processes of the first steps are always carried out at room temperature. Compared with respect to the classical synthesis of conventional ceramics, the sol-gel method minimizes considerably the chemical interactions between the material and the container walls [42]. Furthermore, the size of the particles of sol-gel ceramics can be easily controlled. On the other hand, the sol-gel synthesis of ceramics will never be able to compete for the mass production of some large scale materials.

Many definitions of sol-gel processes exist, and this is due to the fact that is a very studied and used process. In fact, it has to be pointed out that the sol-gel process, no longer includes only oxides but also some other components such as nitrides and sulphides that have been used recently in the synthesis of hybrid organic-inorganic materials. For the purpose of this work, it is considered this process as a colloidal system used to synthesize ceramics with an intermediate stage including a sol and a gel state. As it may be expected, many variations can be brought to the sol-gel synthesis of ceramics. In fact, sol-gel processing does not only designate a unique technique, but a very broad type of procedures [42]. Basically, this technique is achieved in three steps:

- Selecting the precursors of the wanted material. It is the precursor that, by its chemistry, leads the reaction towards the formation of either colloidal particles or polymeric gels.
- The precursor and the solvent are mixed in order to make the solution which turns into the gel.
- The gel heat treatment to obtain the wanted material. This final step is needed to achieve a compact mixture, thanks to the removal of the remaining solvent, and to allow the material crystallization.

The most common use of sol-gel is in coatings devices such as in anti-reflective coatings with index gradation, optical or infra-red absorbing coatings, electrically conductive coatings. It is also used to produce coatings that protect against scratch, oxidation and erosion some types of materials. In parallel with the rise of the interest

for the sol-gel method, the way in which it is applied is increased. For example, one of the method is named *Method of alkoxides* where the the starting reagents are alkoxide. Another one is the *Method with the urea*, which is a sol-gel process that permits the formation of the colloidal suspensions and the gel through the so-called gelling agents. Then, a further method is the *Citrate process* where the citric acid is used as a complexing agent in aqueous solutions of metal salts. However, the chemical details that characterize this process will not be discussed, not being this the aim of this work. To investigate the topic refer to [41].

3.3 Deposition Procedure of Magnesium Oxide

Since the manufacturing process finalized to the coating deposition on the glass substratum has never been made for the present application, it was preceded by several attempts before its optimization. The process has been developed to ensure easy repeatability and greater affordability, searching for the best possible outcome. As previously anticipated, for the secondary emission study the magnesium oxide is one of the most commonly used materials. Furthermore, for the coating realization by the sol-gel method, it was taken into account the raw material cost and the availability, so it was decided to enhance the process using the magnesium oxide.

According to [44], the first step provides for the preparation by the solution composed of the precursor and the solvent. The precursor used for the preparation of MgO coating was magnesium ethoxide (granular, purity $\geq 98\%$). Magnesium ethoxide was dissolved in 2-methoxyethanol (anhydrous, purity $\geq 99.8\%$). In particular a 25 wt% solution was prepared. The mixture is stirred by a magnetic-stirrer for 2 hours. Initially, the work has been directly done on the cylindrical glass tube. The deposition method employed at the start is the easiest and cheapest one. Hence, the various samples have been prepared:

- a specimen has been filled with the solution, it was shaken for a few seconds, then it was emptied and dried at room temperature overnight;
- a specimen has been filled with the solution, it was shaken for a few seconds, then it was emptied and dried at temperature of 75 °C in oven overnight;
- a specimen has been filled with the solution and left at rest at room temperature overnight;
- a specimen has been filled with the solution and left at rest at temperature of 75 °C in oven overnight.

Figure 3.1: The cylindrical glass tube coating prepared according to the four different ways described above.

During the step of drying air moisture, the sol-gel process occurs through the hydrolysis. Then, at this point, the last step of heat treatment has been done. This step of the preparation involves the curing at a temperature of 500 °C in air with a heating ramp of 10 degrees per minute. Then the temperature remains constant for 1 hour, and finally gradually decreases 10 degrees per minute. This step leads to the formation of MgO.

Figure 3.2: The oven used for the heat treatment

To verify the condition of the deposited coating, the Scanning Elctron Microscope (SEM) images have been done using the JSM Jeol 6490 SEM model at the CEASC of University of Padova. In particular, SEM images of the samples in Figure 3.3 were acquired to investigate the thickness and morphology of the layer. Depending on the sol-gel process conditions, a layer of MgO comprised between 0.5 μm and 1 μ m can be obtained. On top of this layer, MgO crystals can be observed, as shown in Figure 3.3.

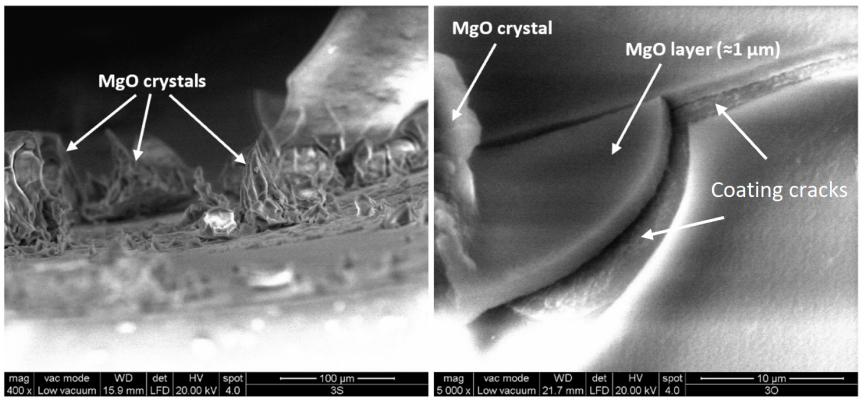

Figure 3.3: SEM images of MgO crystals and layer of the deposited coating.

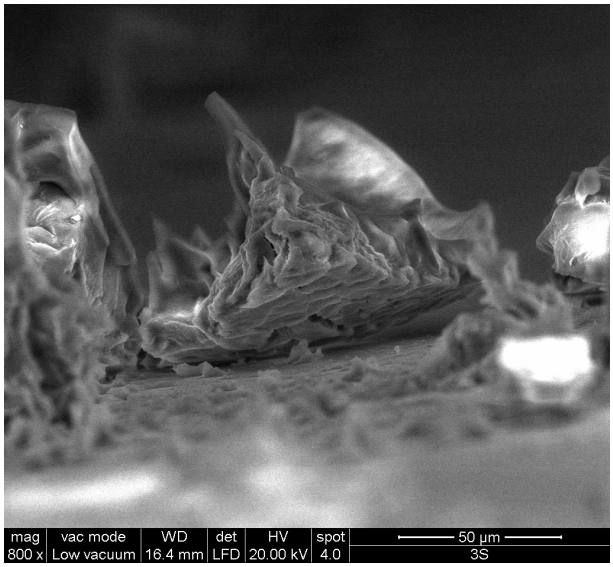

Figure 3.4: SEM image of the MgO layer. The coating detail shows that the layer is raised from the substratum.

The final heat treatment allows the material crystallization, as well as the residual solvent evaporation. Moreover, the type of drying affects the final product characteristics, defining a change of porosity and homogeneity. In the case of this attempt , it can be observed in Figure 3.3 that the film is not uniform and it is not homogeneous. In particular, in the right image, a crack is very evident. The drying phase is the step during which the development of cracks is more likely to occur. This may be caused by the difference in drying time of the sol-gel that can be introduce stress. The pores with a greater dimension dries quicker than the smaller sized pores, due to the highest vapour pressure of the liquid.

In addition to the surface tensions caused by the heat treatment, the probable reason why the layer is characterised by many cracks is that the weight percentage

of the solution is not appropriate. The procedure followed is indeed aimed to the production of fibres [44]. For this reason, a 5 wt% solution has been prepared. Furthermore, in Figure 3.4 it can be noticed that a part of the coating is raised from the substratum, which means that it has not adhered properly. For this last problem, it was used the chemical functionalization of the surface.

The surface functionalization aims to modify the chemical composition of the surface by integrating elements or functional groups which may enhance the adhesion of the layer to the glass. By obtaining as more $-OH$ groups as possible on the substrate surface. So, a solution known as *basic Piranha* is used to achieve a chemical attack. For the glass surface case, the basic piranha mixture is particularly appropriate and is prepared as described below. This solution is composed of a strongly oxidising reagent ammonia NH_3 25 % in aqueous solution, hydrogen peroxide H_2O_2 40 % in aqueous solution. The molar fractions are $NH_3 : H_2O_2 : H_2O = 1 : 3 : 9$ [45]. The solution has been heated until reaching the temperature of 70 °C and left at this temperature for 20 minutes. The quite high temperature facilitates the kinetics of the reaction, increasing the oxidation level and the performance of the basic piranha. In fact, at high temperature, the piranha solutions employ a strong oxidizing attack over the surface and they produce active sites of the $-OH$ type. The formation of these groups is especially advantageous for the chemical bond with other molecules. A second consequence, but nonetheless important for the following coating deposition, is the improvement of the surface wettability.

Each sample was immersed for 20 minutes at a temperature of 70 °C over a hot-plate. The specimens are left in a container filled with distilled water until use, thereafter they are dried with a compressed air jet. At this point, the 5 wt% solution has been prepared and the coating has been deposited on the samples, repeating the cases previously shown.

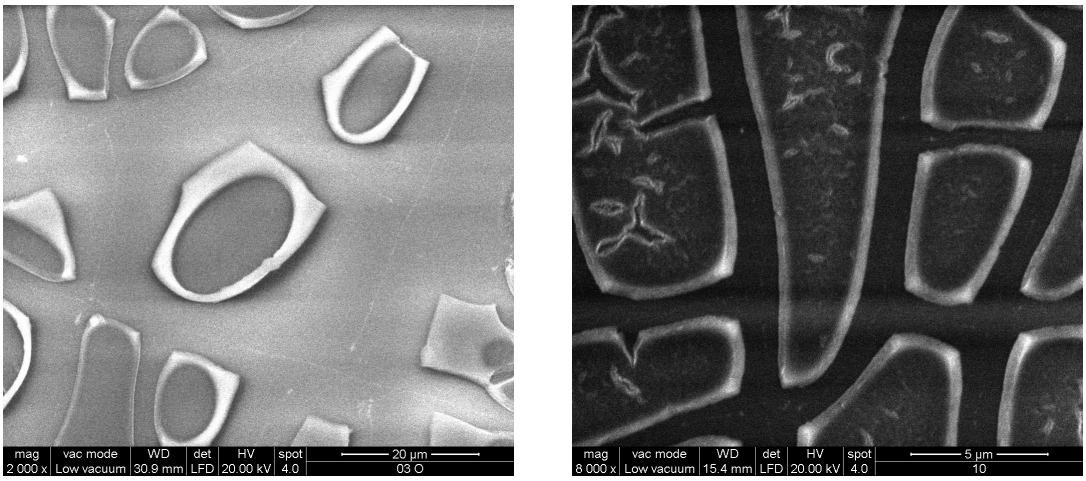

Figure 3.5: SEM images of the MgO coating after the use of basic piranha solution. In this case a 5 wt% solution was prepared.

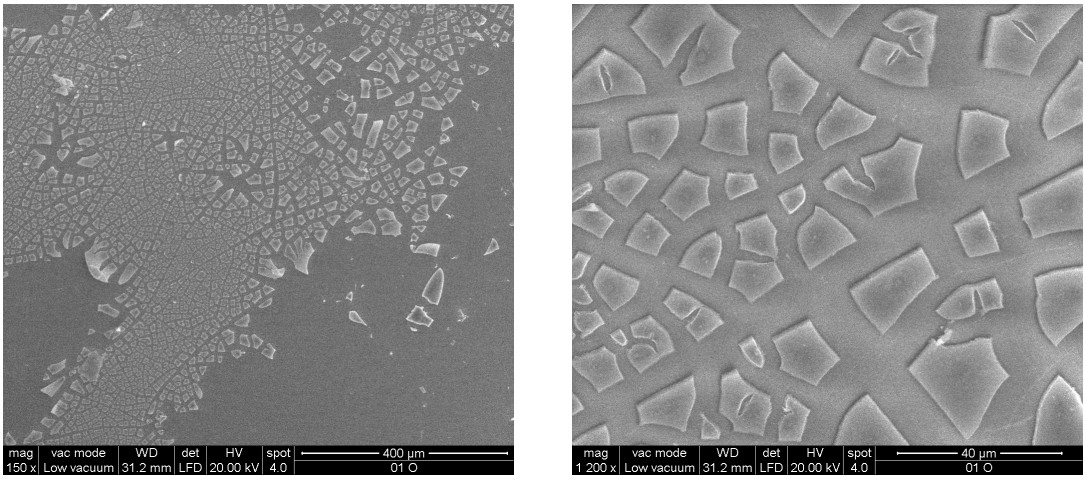

Figure 3.6: SEM images of the MgO coating after the use of basic piranha solution. In this case a 5 wt% solution was prepared. The figure shows many areas where the coating has not adhered and the presence of many cracks.

From SEM images shown in Figure 3.5, it can be noticed that the central region of the coating has well adhered, and this can be deduced by the fact that this area is darker. Unfortunately, even though the expedients, there are still many areas where the coating has not properly adhered. Also, from Figure 3.6 it is evident that the obtained layer is not uniform and there are still many cracks.

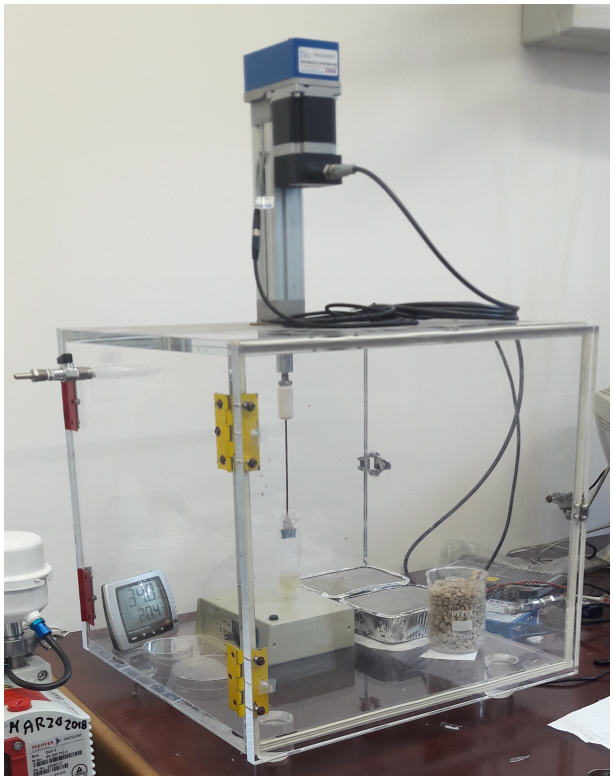

Figure 3.7: Instrument for the dip coating method of deposition.

To enhance the morphology and to produce layer with different thickness, it has been decided to change the previous deposition method with the so-called *dip coating method*. This process is used to create thin films over a solid substrate by the sample immersion in a container including the material in a liquid state to deposit. This is followed by the removal and drying. The dip coating method includes the use of dedicated machinery shown in Figure 3.7. This device works in a controlled humidity environment. The specimen is connected to a support (Figure 3.8), which in turn is moved by a piston. The piston velocity is controlled remotely. Then, since the velocity with which the sample is immersed in the solution is selected and rests constant, it is possible to obtain a more homogeneous coating. Indeed, also the thickness should be constant over the whole specimen.

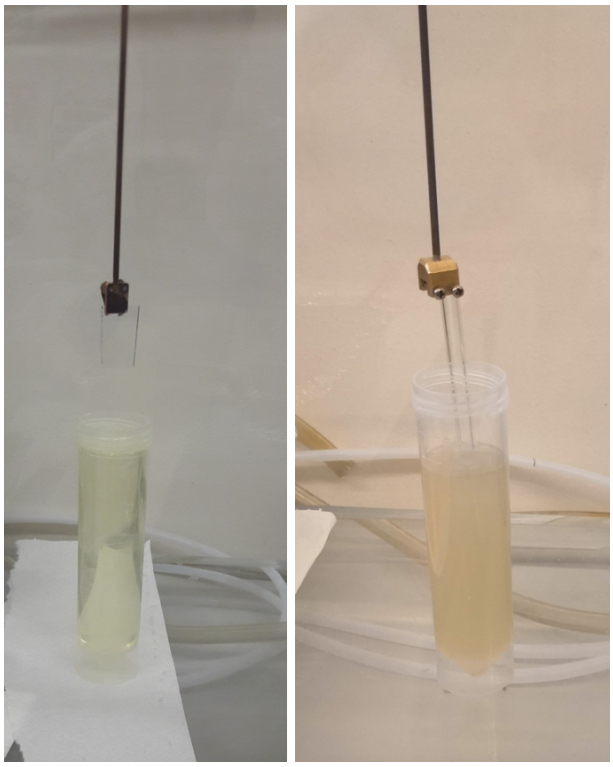

Figure 3.8: In the figure the support at which the sample is connected during the dip coating process is shown.

To know the correct value of the coating thickness which has been deposited, the samples were analysed using a using a KLA-Tencor P-16+ contact profilometer. The KLA-Tencor P-16+ profilometer exploits a diamond stylus pressed on the sample and moved along a direction for a specified distance and specified contact force. It can measure small variations of the stylus along the vertical direction which are directly correlated to the surface morphology of the sample. The height position of the diamond stylus chances due to the surface morphology and it is converted to an analogic signal by means of a piezoelectric transducer; finally, this signal is converted into a digital signal. Profilometer scans can be 200 mm long with a

vertical resolution of few nanometres and a vertical range up to 1 mm. To ease the profilometer measurement, the coating will be deposited not only on the glass tube, but also over a slide, made in soda-lime glass. At this point, after the sample has been dipped into the solution, it was left to dry at room temperature for a few minutes. Then, the specimen has been endured a heat treatment which consists in a heating ramp of 10 degrees per minute until to reach the temperature of 500 °C. Then the temperature remains constant for 1 hour, and finally gradually decreases 10 degrees per minute. The results obtained for three different velocities, namely (i) 10cm/min, (ii) 20 cm/min, and (iii) 40 cm/min, are shown below.

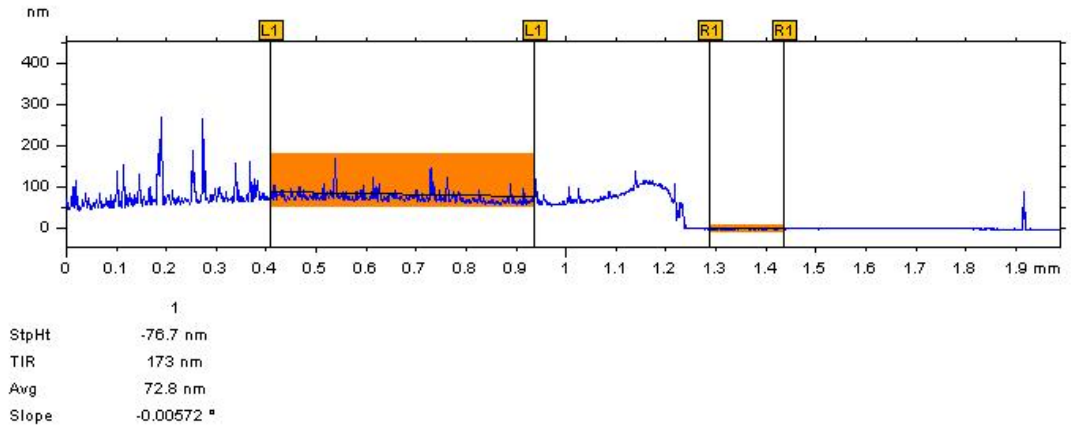

Figure 3.9: Profilometer analysis result for the dipping velocity of 10 cm/min. The thickness of the MgO layer is 76.7 nm.

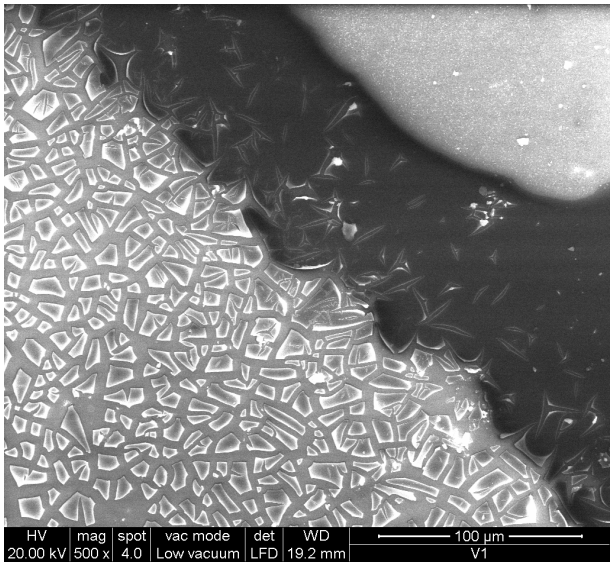

Figure 3.10: SEM image of the MgO coating prepared with 10 cm/min dipping velocity. The coating presents several cracks, but there are many areas where the layer has adhered, i.e. the darker parts in the layer pieces.

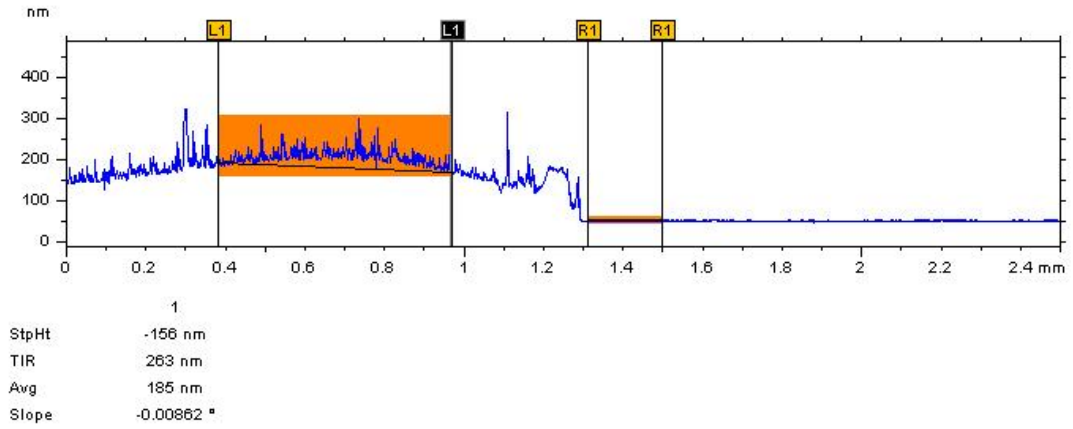

Figure 3.11: Profilometer analysis result for the dipping velocity of 20 cm/min. The thickness of the MgO layer is 156 nm.

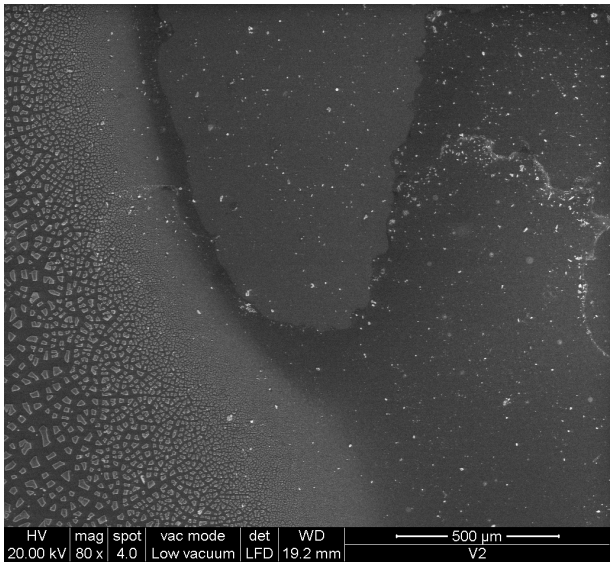

Figure 3.12: SEM image of the MgO coating prepared with 20 cm/min dipping velocity. The layer is characterized by many cracks, as expected increasing the dipping velocity.

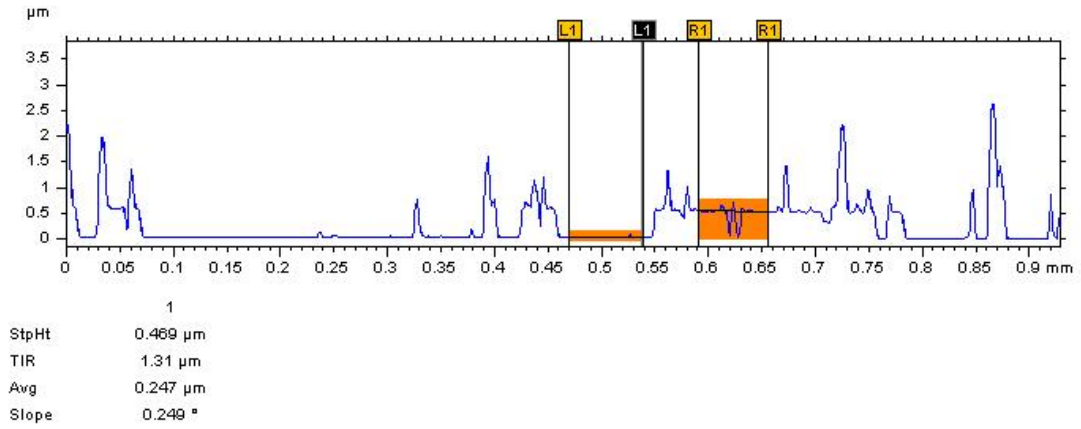

Figure 3.13: Profilometer analysis result for the dipping velocity of 40 cm/min. The thickness of the MgO layer is 470 nm.

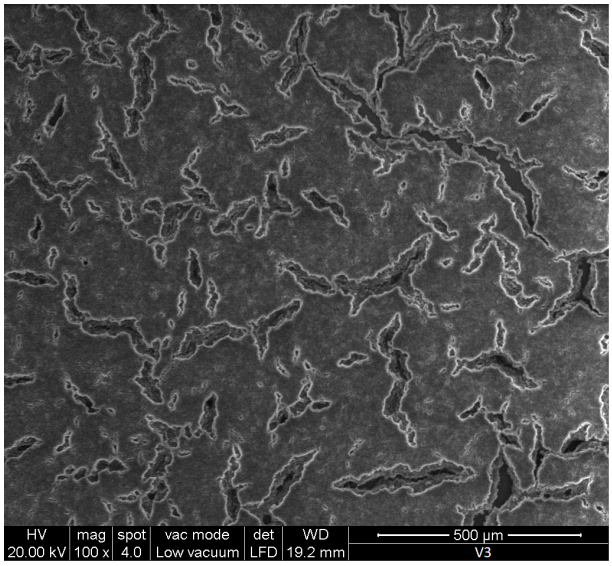

Figure 3.14: SEM image of the MgO coating prepared with 40 cm/min dipping velocity.

The first dipping velocity of 10 cm/min results in a lower thickness with respect to the other 2 velocities, as expected. In particular, from the profilometer result shown in Figure 3.9, the thickness value of the coating deposited with the 10 cm/min dipping velocity is 76.7 nm. The thickness over the whole sample is not constant, probably due to the specimen position during the drying and curing phases. Analysing the SEM image in Figure 3.10 it can be noticed that the coating is characterized by several cracks. However, there are many areas where the layer has firmly adhered.

Increasing the dipping velocity, the layer thickness accordingly enhances. Nevertheless, also the possibility that the coating has less adhered to the substrate might

increase. Using the dipping velocity of 20 cm/min the resulting thickness is of 156 nm. As it is shown in the SEM images Figure 3.12, the presence of many cracks is evident also in this layer. This is probably due to the granular state of the magnesium oxide precursor, not only by the heat treatment.

The layer obtained with a velocity of 40 cm/min has a thickness of 470 nm. The thickness of the layer can affect the resulting SEEY. In literature, coatings with thickness of the order of 10 to 100 nm are more common [39], [34], [38]. For this reason, no vessels have been produced with a dip coating velocity higher than 20 cm/min. Moreover, a greater layer thickness may affect the adhesion of the layer to the substrate that could easily detach during the work operation.

3.4 Deposition Procedure of Titania and Alumina

In the present section the results concerning the coating of Titania (TiO_2) and Alumina (Al_2O_3) will be presented. The different steps, which have been carried out to realize these layers, follow the procedure described in the previous section and here briefly reminded. First of all the samples have been exposed to the chemical attack by means of the basic piranha solution. Each glass samples was immersed in the mixture for 20 minutes at temperature of 70 °C over a hot-plate. So, the specimens are left in a container filled with distilled water until use, thereafter they are dried with a compressed air jet. Therefore, the two precursor solutions have been prepared always using the sol-gel method.

As regards the alumina, the solution composed of the precursor, the solvent and the chelating agent has been prepared as described in [43]. In particular, aluminum tri-sec-butoxide ($Al(O-sec-Bu)_3$ liquid, purity 97%) was used as precursor, isopropyl alcohol ($i-PrOH$ purity $\geq$ 99.7%) was used as solvent, while ethyl acetoacetate ($EcAcAc$, $CH_3COCH_2COOC_2H_5$ purity $\geq$ 99.0%) was chosen as the chelating agent. The aluminum tri-sec-butoxide and the isopropyl alcohol were mixed and stirred at room temperature for about 1 hour. The ethyl acetoacetate was added to the solution and the solution was stirred for 3 hours. $i-PrOH$ diluted in water was then carefully added to the solution for hydrolysis. The solution obtained was used for the coating. The molar ratios of $i-PrOH$, $EcAcAc$, and H_2O to $Al(O-sec-Bu)_3$ were 20, 1, and 4, respectively. The specimens have been dip coated with the solution, using the machine showed in Figure 3.7. In this case, the 10 cm/min dipping velocity of the first layer has been set. At this point, after the sample has been dipped in the solution, it was left to dry at room temperature for a few minutes. Then, the specimen has been endured a heat treatment which consists in a heating ramp of 10 degrees per minute until to reach the temperature of 500 °C. Then, the temperature remains constant for 1 hour, and so gradually decreases 10 degrees per minute. This step leading to the formation of Al_2O_3. After the achievement of the first layer, a second layer of alumina has been deposited on the sample sample with a velocity of 5 cm/min. It was chosen to realize the second layer with a lower value of velocity, since the substrate, in this case, is made of the

same material, i.e. alumina. So, it has been supposed that the the second layer has an increased adherence compared to the first one. Then, to avoid too high coating thickness, the decision just discussed above has been made. At this point of the process, the specimen has been exposed to the second heat treatment, identical to the first. The results obtained for the alumina coating are shown below.

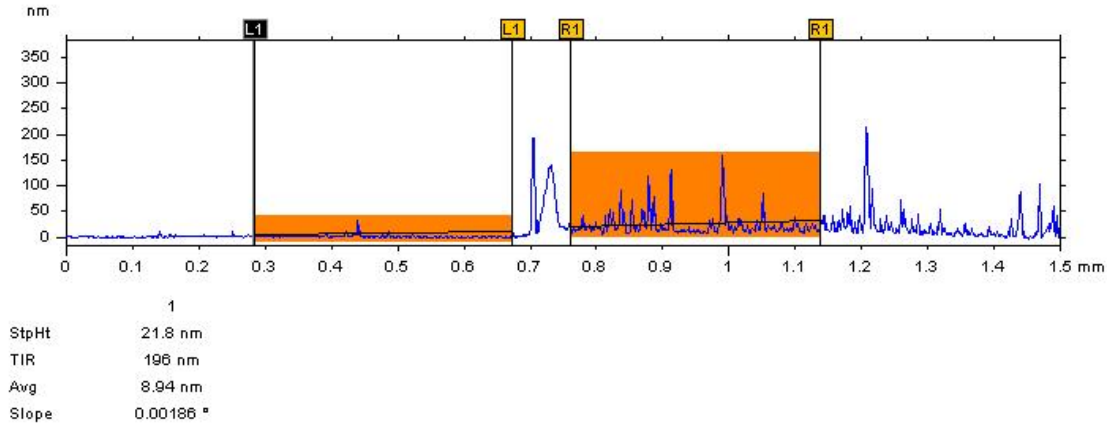

Figure 3.15: Profilometer analysis result for the first layer dipping velocity of 10 cm/min. The thickness of the Al_2O_3 first layer is 21.8 nm.

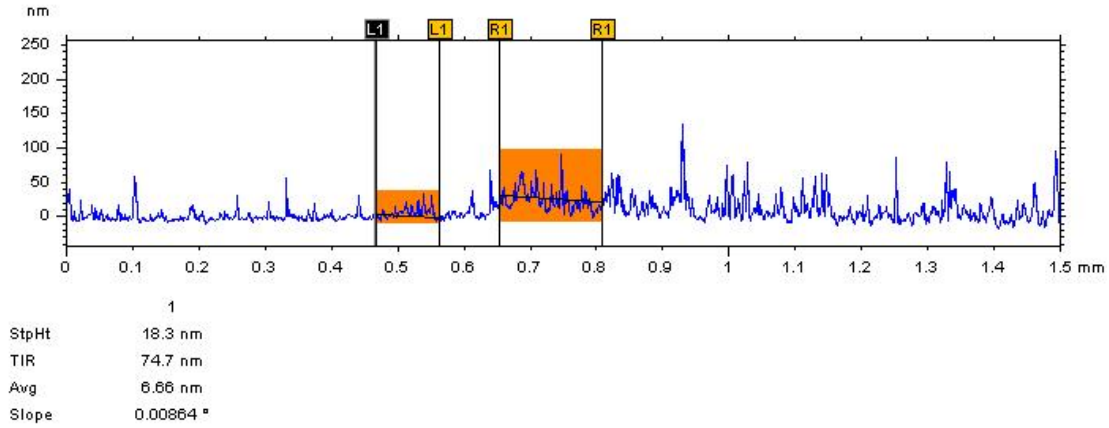

Figure 3.16: Profilometer analysis result for the second layer dipping velocity of 5 cm/min. The thickness of the Al_2O_3 second layer is 18.3 nm.

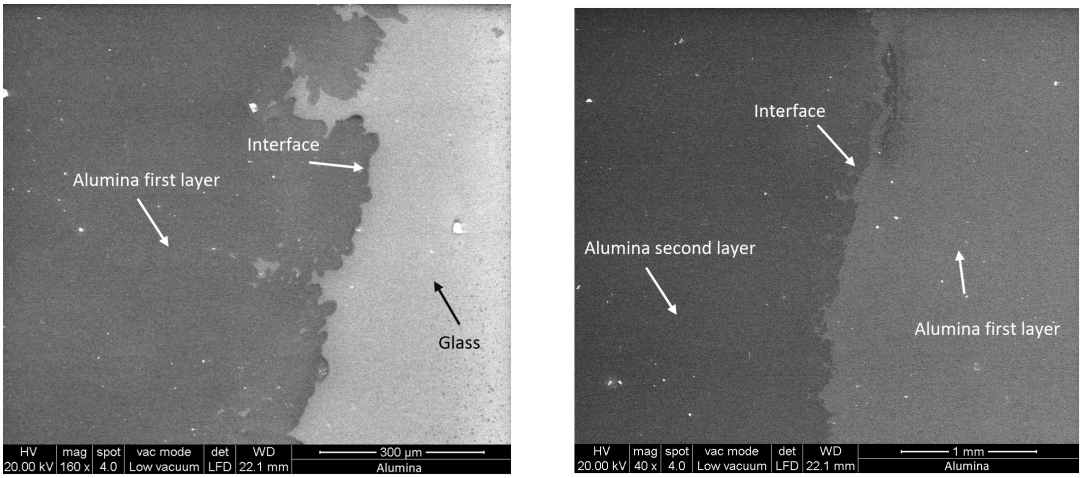

a) b)

Figure 3.17: a) SEM image of the interface between the glass and the first layer of Al_2O_3 coating, which it is deposited with a dipping velocity of 10 cm/min; b) SEM image of the interface between the first and the second layer of Al_2O_3 coating. The latter was obtained with dipping velocity of 5 cm/min.

The result obtained by the profilometer analysis is shown in Figure 3.15 and it explained that the thickness of the alumina first layer, which has been deposited, is 21.8 nm. In the SEM image in Figure 3.17 a) the interface between the glass substrate and the first layer can been easily seen. In fact, the brighter area in the right side coincides with the glass substrate, instead in the left side the first layer of alumina is distinctly visible. The second layer has a 18.3 nm value of thickness, as indicated in Figure 3.16. Also in this case it is possible to identify the interface between the first and second layer, as shown in Figure 3.17 b). As it can be noticed from the previous SEM images, the coating seems to be uniformly distributed and also it does not present any areas with cracks, except for the interface area. The layer is adhered more firmly and it presents a more uniform morphology compared to the MgO coating, probably because the layer thickness is thinner and the precursor that is used in this case is in a liquid state. It is helpful compares these results with those of the MgO. By comparing Figure 3.10 and Figure 3.17, several differences between the magnesium oxide layer and the alumina layer can be noted. MgO layer presents several cracks with respect to the Al_2O_3 layer.

The last coatings have been realized with titania (TiO_2), and with multilayered $MgO - TiO_2$, as suggested in literature [35]. As it has been done in the previous case, the specimens have been exposed to the chemical attack by means of the basic piranha solution. Each glass samples was immersed in the mixture for 20 minutes at temperature of 70 °C over a hot-plate. So, the specimens are left in a container filled with distilled water until use, thereafter they are dried with a compressed air jet. Then, the solution to obtain the titania has been prepared using the sol-gel method. Firstly, a stock solution has been prepared and it is composed of 4.5

ml of titanium (IV) isopropoxide ($Ti(OC_4H_9)_4$ liquid, purity $\geq$ 97%), 10 ml of n-propanol (C_3H_8O anhydrous, purity $\geq$ 99.5%) and 1.6 ml of acetil acetone ($AcAc$, $CH_3COCH_2COCH_3$ purity $\geq$ 99%). The obtained mixture was mixed and stirred at room temperature for about 1 hour. At this point, a casting solution has been achieved. A solution of 1.613 ml of n-propanol and 0.187 of water is added for any 1 ml of the stock solution. This last is added to the stock solution and the whole mixture was mixed and stirred at room temperature for about 2 hours. When the solution was ready to use, the coating over the specimens has been deposited by the dip coating machinery. Also in this case the double layer of TiO_2 and the multi-layered di $MgO - TiO_2$ have been realized. By following what has been previously done, the dipping velocity for the first coat is 10 cm/min. When the first layer was deposited, the samples have been endured a heat treatment which consists in a heating ramp of 10 degrees per minute until to reach the temperature of 500 °C. Then, the temperature remains constant for 1 hour, and so gradually decreases 10 degrees per minute. This step lead to the formation of TiO_2 in one case, and MgO in the other. Therefore, the second coating has been deposited, and in the both cases the coating is made of titania. The dipping velocity used for the second layer is 5 cm/min. So, the samples have been endured at the second heat treatment. The results obtained for the titania coating are shown below.

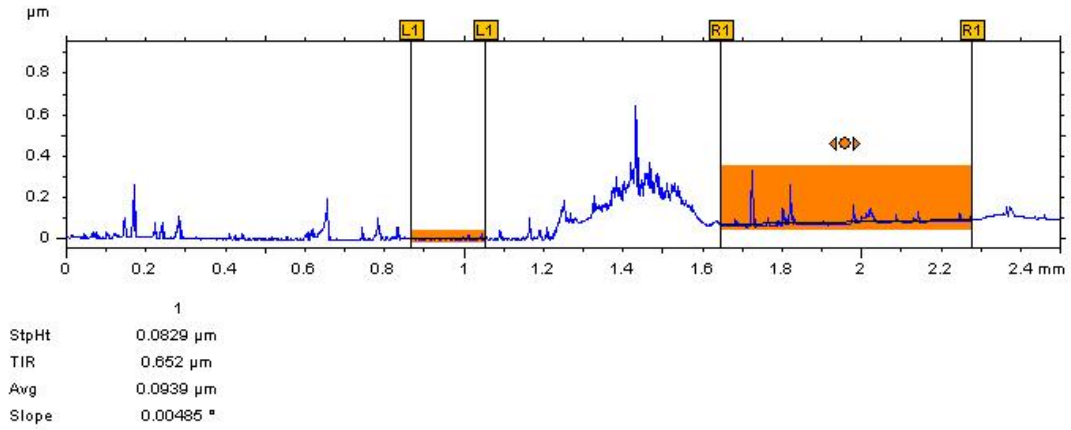

Figure 3.18: Profilometer analysis result for the first titania layer dipping velocity of 10 cm/min. The thickness of the TiO_2 second layer is 82.9 nm.

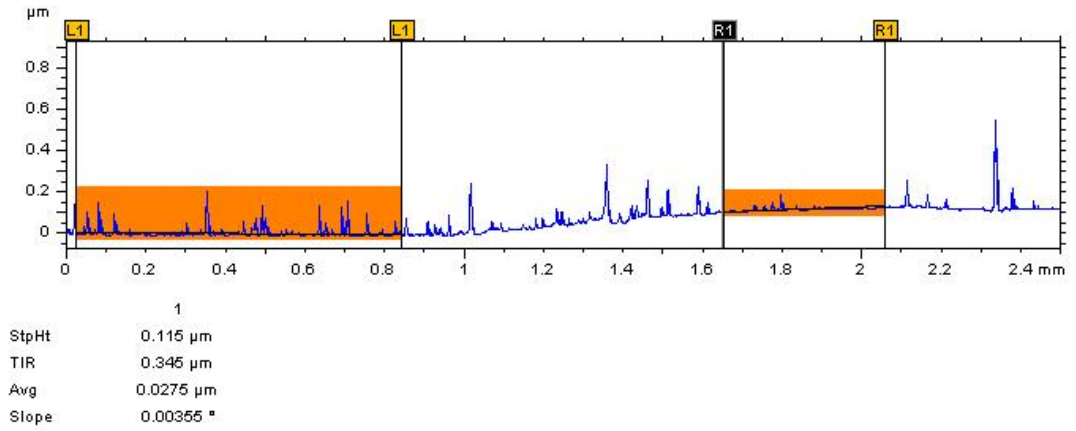

Figure 3.19: Profilometer analysis result for the second titania layer dipping velocity of 5 cm/min. The thickness of the TiO_2 second layer is 115 nm.

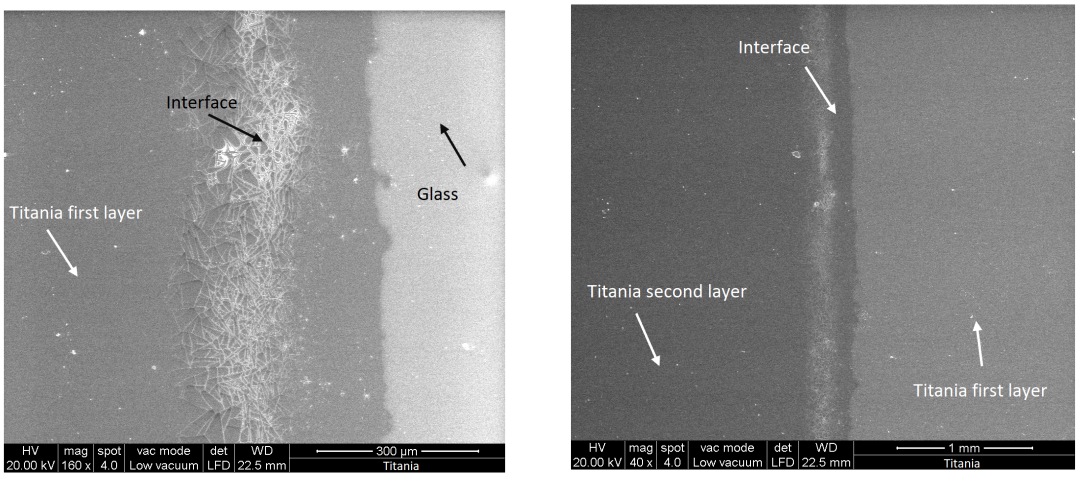

a) b)

Figure 3.20: a) SEM image of the interface between the glass and the first layer of TiO_2 coating; b) SEM image of the interface between the first and the second layer of TiO_2 coating.

In Figure 3.18 is shown the results obtained by the profilometer analysis and it is illustrated that the first layer thickness of titania is 82.9 nm. In the SEM image in Figure 3.20 a) the interface between the glass substrate and the first layer can been easily seen. Indeed, the brighter area in the right side coincides with the glass substrate, instead in the left side the first layer of titania is distinctly visible. The second layer has a 115 nm value of thickness, as indicated in Figure 3.19. Also in this case it is possible to identify the interface between the first and second layer of TiO_2, as shown in Figure 3.20 b). As can be noticed from the previous SEM images the coating is characterized by several cracks, as it is shown in detail in Figure 3.21.

Nevertheless, the cracks are limited to the interface area. Indeed, the remainder of the coating is rather uniform and the thickness is constant.

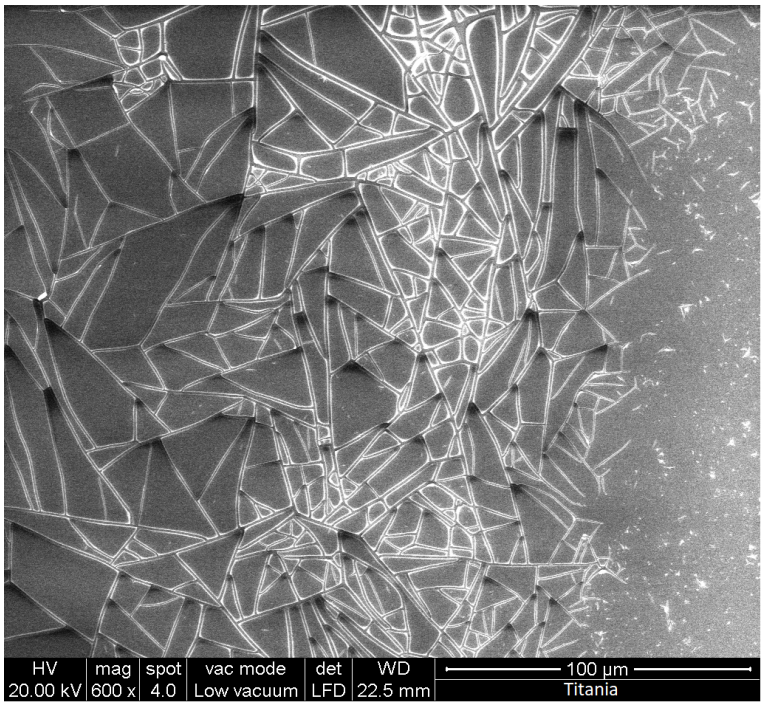

Figure 3.21: SEM image which shows a detail of the interface area. The interface zone is characterized by several cracks, but they are limited in this area.

Concerning the multilayered $MgO - TiO_2$, the obtained results have been shown below.

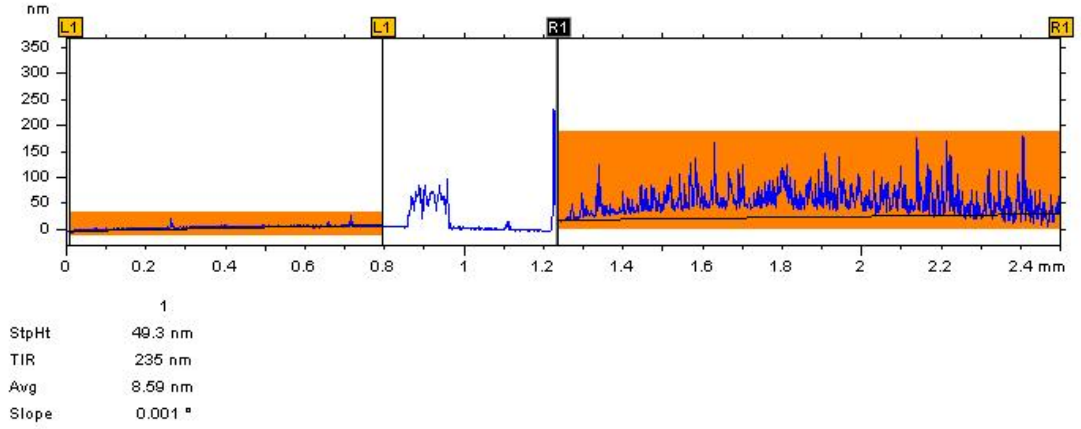

Figure 3.22: Profilometer analysis result for the first MgO layer dipping velocity of 10 cm/min. The thickness of the MgO layer is 49.3 nm.

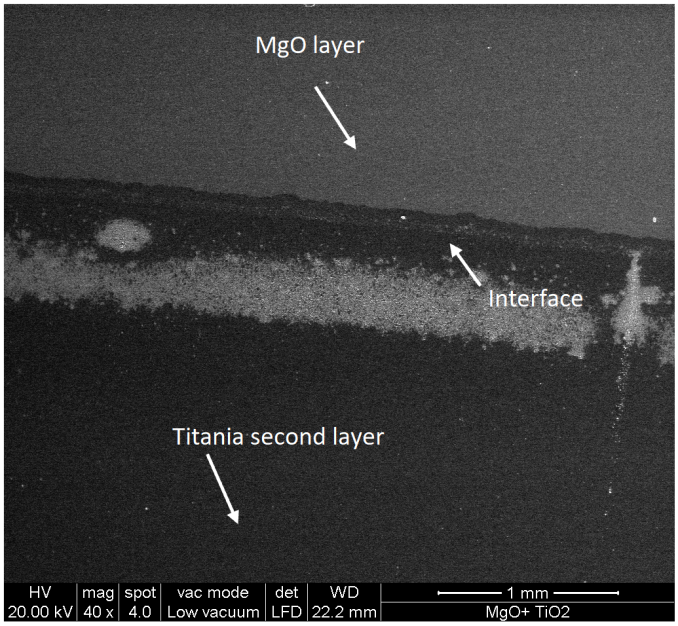

Figure 3.23: SEM image of the interface between the layer of MgO and the second layer of TiO_2. The coating has adhered uniformly.

Unfortunately, by the profilometer analysis it has been possible to detect only the thickness of MgO, which is equal to 49.3 nm, as it is shown in Figure 3.22. Whereas, from the SEM images in Figure 3.23, it can be observed that the titania layer was deposited and it has adhered uniformly.

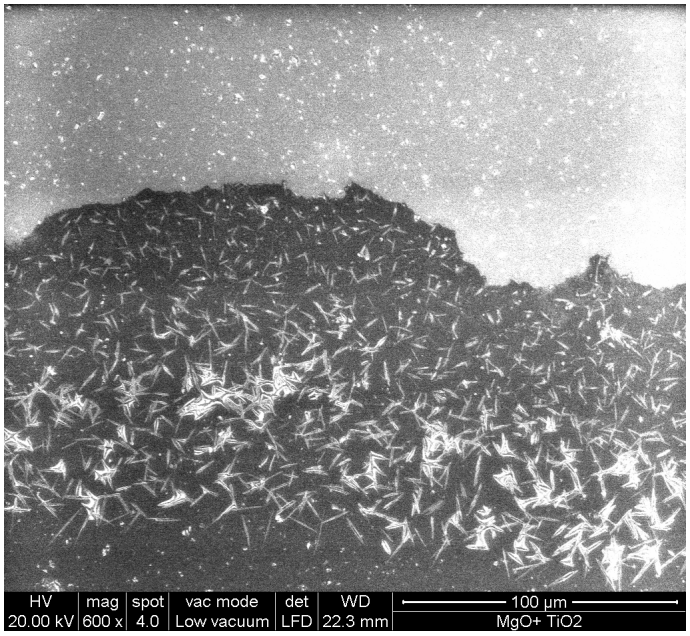

Figure 3.24: SEM image which shows a detail of the interface area. The interface zone is characterized by several cracks, but they are limited in this area.

Also in this sample, the coating is characterized by several cracks in the interface area (detail in Figure 3.24), between the first coat of MgO and the second layer of titania. These cracks are probably caused by an accumulation of material in the interface zone during the drying and the heat treatment phase.

Then, this last described procedure is the method which is used to deposit the coating over the cylindrical tube glass. This last will be welded in the central section of the vessel. In particular, the follow samples have been achieved:

- the monolayer of MgO deposited with the dipping velocity of 10 cm/min;
- the monolayer of MgO deposited with the dipping velocity of 20 cm/min;
- the double layer of MgO;
- the double layer of Al_2O_3;
- double layer of TiO_2;
- the multilayered of $MgO - TiO_2$.

CHAPTER 4

Experimental Setup and Results

This Chapter will firstly introduce the test equipment and procedures that are going to be used to performed the experimental work.
Secondly, the outcomes of data analysis with the purpose to show which direction further research and development should follow in order to keep improving gaseous plasma antenna technology has been presented.

4.1 Testing and Instrumentation

The parameter that has been measured to evaluate the performance of plasma discharge is the plasma density. The bench equipment comprises a power supply and a microwave interferometer, developed by CISAS [46].

The high frequency generation method relies on a commercial high voltage transformer, connected to two CCFL electrodes immersed at the end of the glass vessel, and thus in contact with the gas, and the plasma itself. The transformer is a MIDI ECG 2100 model Tecnolux (Figure 4.1) and the technical features of the device are listed in Table 4.1. This transformer was found to absorb 30 W from the wall socket during testing.

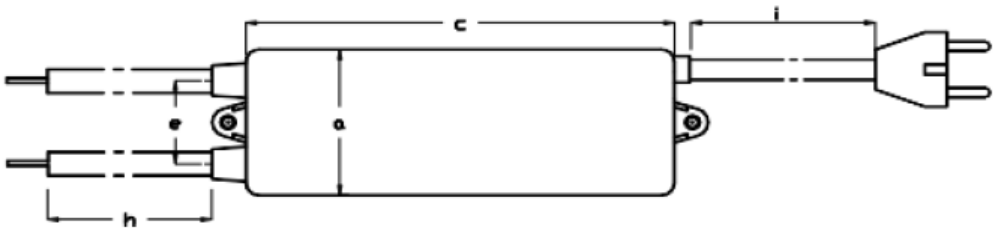

Figure 4.1: MIDI EGG 2100 power supply.

Parameter	Value
Input Voltage	200-250 V
Input Current	Up to 400 mA
Input Power	Up to 90 W
Input Frequency	50-60 Hz
Output Voltage	2 kV max
Output Short-circuit Current	95 mA
Output Current to Load	84 mA (nominal)
Output Frequency	19 kHz

Table 4.1: The MIDI EGG 2100 features.

The phase jump is measured by means of a phase comparison between a sample microwave signal and the wave that is driven through the vessel. The different length of the path is already accounted for through calibration, except for the delay introduced by the plasma inside the vessel. The phase difference can then be used to estimate the electron density within the vessel.

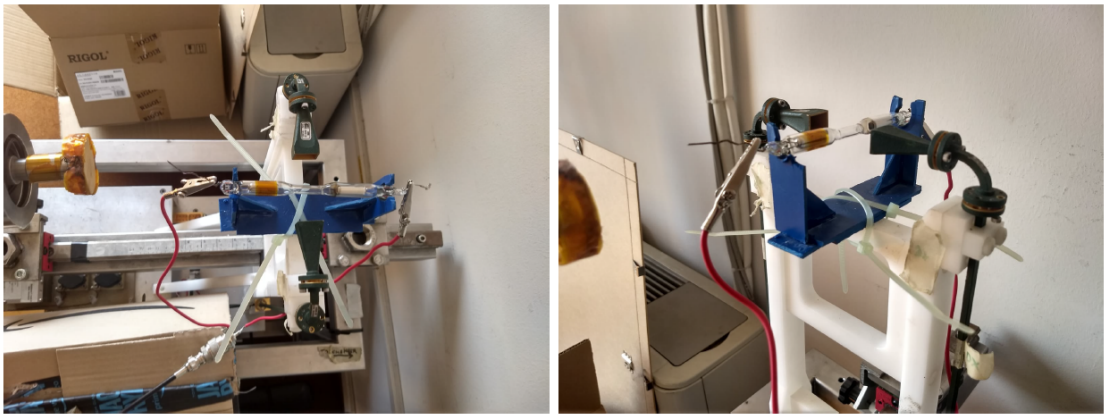

Figure 4.2: a) The view from above of the vessel position on the plastic support. b) The view from side of the vessel position on the plastic support.

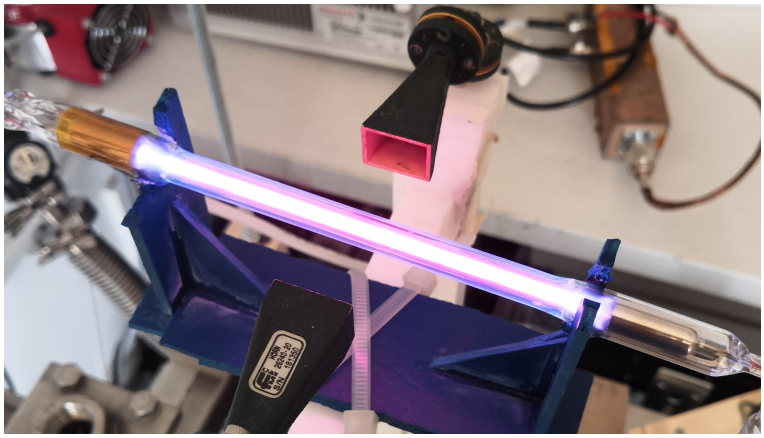

Figure 4.3: Picture of the vessel in the "on" state.

A dedicated PC runs the acquisition manager (Figure 4.4), from which it is possible to launch the measurement. The user has to manually launch the measurement, whereas the end is set automatically by the acquisition time value.

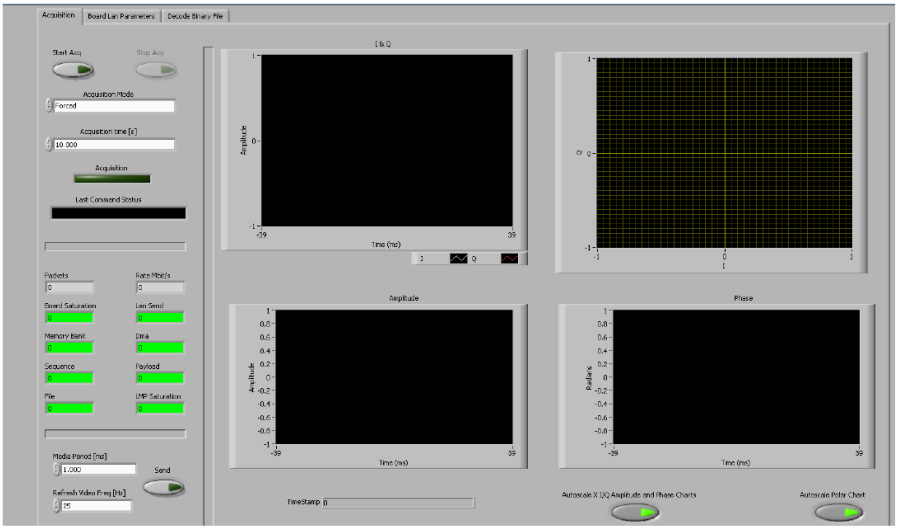

Figure 4.4: Acquisition manager.

The measurements is carried out through the use of an interferometer and a phase comparator, the former is set to a frequency of 75 GHz. At this working frequency, a noise contribution of 0.1° will create a variation in density of $\approx 10^{16}$ $\frac{\#particles}{m^3}$. On the other hand, a 2π phase shift is achieved when $N \approx 2.8 \cdot 10^{19}$ $\frac{\#particles}{m^3}$. Therefore, the instrument is able to measure densities (in this configuration) up to $N \approx 1 \cdot 10^{19}$ $\frac{\#particles}{m^3}$ with a 4 % of error [46]. Due to the high sensitivity of the experiment to vibrations, the wave guides have been tightly secured to the support structure, and post processing HF filtering smooths the spectrum (vibrations introduce stray components above 100 Hz). This discussion highlights the importance of accurate

phase difference measurements, as the phase jump generated by an abrupt temporal discontinuity in plasma density (i.e. turning off/on the discharge) can be linked numerically to said parameter, as explained in [46].

4.1.1 Density Measurements Procedures

These tests are at point fixed in voltage and the power is delivered by using the transformer which is shown in Figure 4.1.

1. Carefully place the plasma discharge on the plastic support, making sure the wave from the interferometer goes through the centre of the vessel.
2. Connect the crocodile clips from the MIDI ECG 2100 to the wires sticking out of the glass enclosure. Polarity is not important but it is preferable to keep the procedure as similar as possible for each repetition.
3. Move on and prepare the PC for acquisition then start the acquisition.
4. Turn on the discharge from the switch on the power supply socket.
5. Turn off the discharge through the same switch.
6. Now it is possible to save the output file from the interferometer through the acquisition program.
7. Turn off the power supply (if via the another vessel has to be tested afterwards).

4.1.2 Post-Processing

Data analysis is performed thanks to the use of MatLab scripts:

- Interferometer AmplitudeAndSlope.m converts the phase data from the interferometer (txt files) into a density measurement, as explained in [46]. The use of properly tuned conversion factors and by filtering of the input data allows to obtain a matrix composed of density data, the maximum density, the minimum density and raw phase jump. The script takes the derivative of the phase data and looks for the maximum value. Then, it identifies the point in time when the jump happened and computes the density value from the difference in the phase before and immediately after the jump. The final matrix is then exported as xls file.
- plotData.m is used to plot relevant quantities and usually requires quite some tweaking if the measurement technique varies.

4.2 Results

In this Section, the tests results are shown. Density tests are performed as explained in Section 4.1.1 and their outcome is to evaluate the density of electrons within the vessel in terms of quantity, reliability and consistency. Moreover, degradation tests have been made to evaluate the vessel performances of plasma discharges for longer ignitions. The procedures of this type of tests are the same as the density measurements. The tests concerning the vessel made of glass (the benchmark) and the vessels characterized by the coatings are presented. To analyse the plasma behaviour, the different coated vessels are compared with the benchmark, with the aim of highlighting the differences from the uncoated case. The following coated vessels have been tested:

- the monolayer of MgO deposited with the dipping velocity of 10 cm/min (Figures 4.9 to 4.12);
- the monolayer of MgO deposited with the dipping velocity of 20 cm/min (Figures 4.13 to 4.16);
- the double layer of MgO (Figures 4.17 to 4.20);
- the BN sprayed coating (Figures 4.21 to 4.24)

To analyse the plasma behaviour of the several cases, two types of diagrams have been considered. The phase plot shows the phase jump for the ignition and the shutdown states, measured as described in Section 4.1, in function of the duration time of the test. The most representative diagram related to via at one test for each vessel has been reported. From the phase jump the value of the ignition and shutdown densities have been acquired, as reported in Section 4.1. Then, the second type of diagram shows the value of the plasma density for ignition and shutdown states obtained for every following test on the same vessel. From this diagram it is possible to evaluate the mean value of the density and to investigate the plasma stability. In order to assure reliability of the results and to allow good level of stabilization as well as assuring some ageing of the plasma discharge, for the duration test of 20 s 30 repetitions have been implemented. So, assuming that the plasma was already stable, for the duration tests of 30 s 10 repetitions have been done.

4.2.1 Benchmark

In this Section the tests results concerning the vessel made of glass are shown. The phase plots and the diagrams of the plasma density are presented.

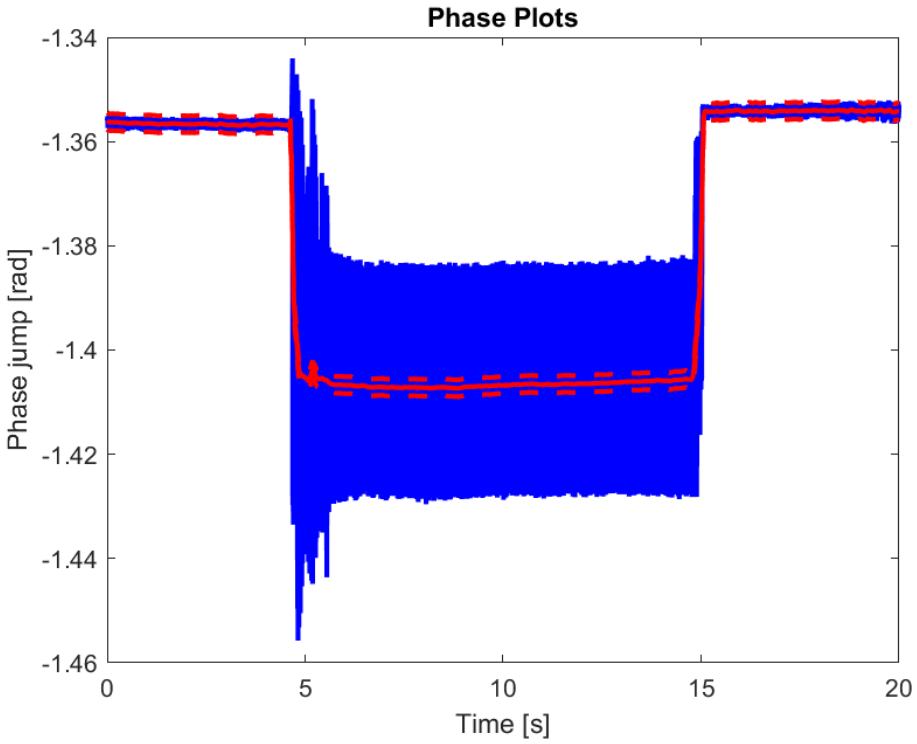

Figure 4.5: Phase plot for the benchmark vessel for a 20 seconds density test. Qualitative analysis of the phase jump at the beginning and end of the density test. X-axis reports the time scale, Y-axis reports the phase value.

Figure 4.6: The benchmark density values for 20 seconds ON-OFF tests. X-axis reports the test sequence, Y-axis reports the density value. Measurement error on the density of $\approx$ 10 %.

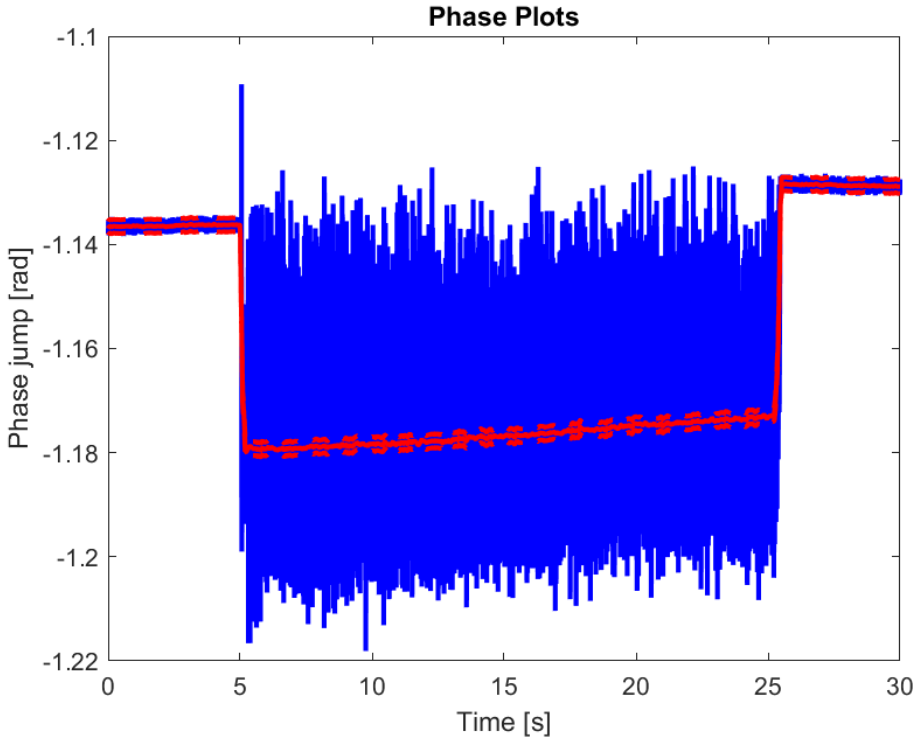

Figure 4.7: Phase plot for the benchmark vessel for a 30 seconds density test. Qualitative analysis of the phase jump at the beginning and end of the density test. X-axis reports the time scale, Y-axis reports the phase value.

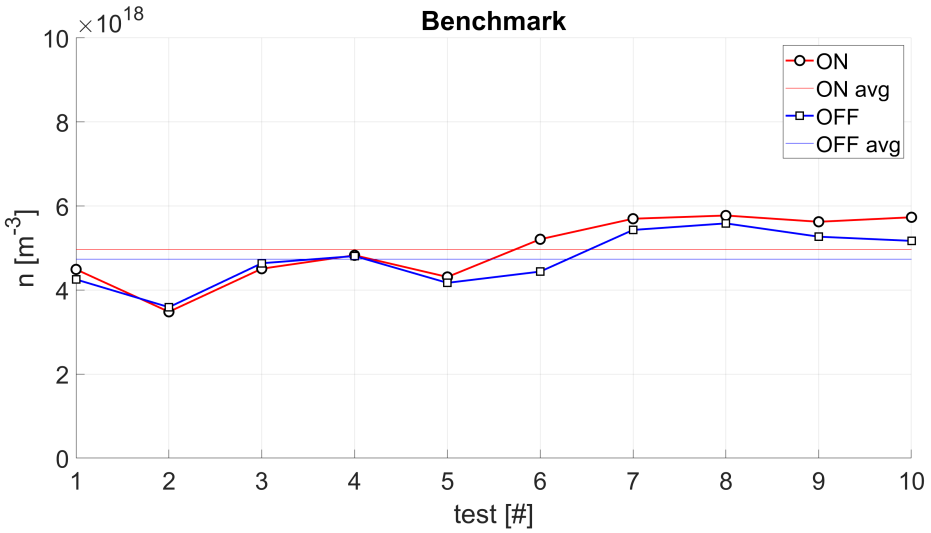

Figure 4.8: The benchmark density values for 30 seconds ON-OFF tests. X-axis reports the test sequence, Y-axis reports the density value. Measurement error on the density of ≈ 10 %.

4.2.2 MgO monolayer - V=10 cm/min

In this Section the tests results concerning the vessel characterized by a single layer MgO coating with a dipping velocity of 10 cm/min are shown. The phase plots and the diagrams of the plasma density are presented.

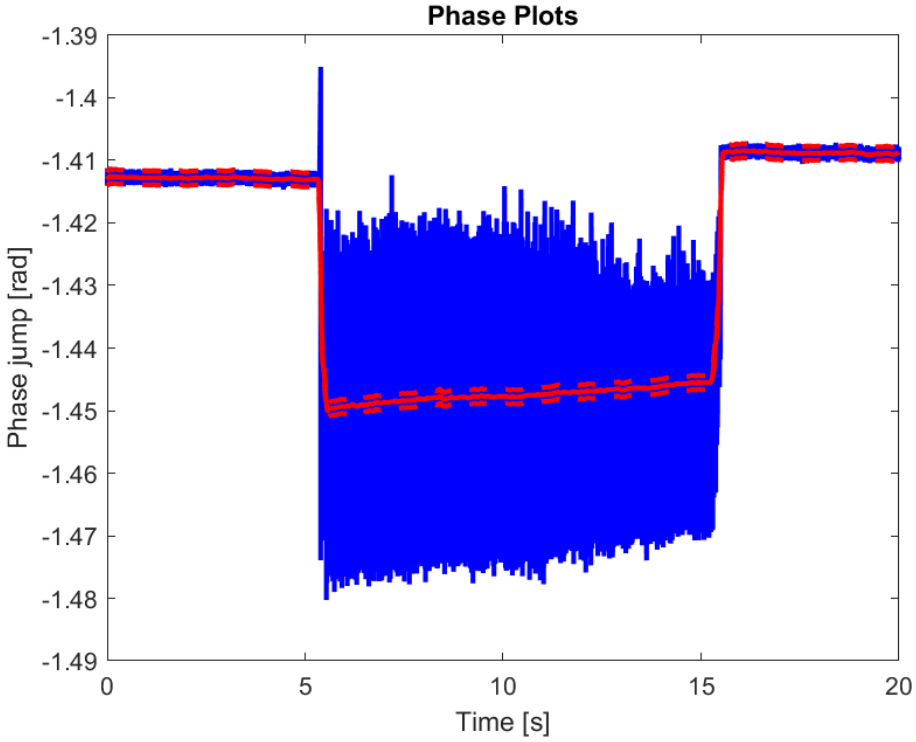

Figure 4.9: Phase plot for the vessel characterized by the MgO coating with a dipping velocity (V1) of 10 cm/min for a 20 seconds density test. Qualitative analysis of the phase jump at the beginning and end of the density test. X-axis reports the time scale, Y-axis reports the phase value.

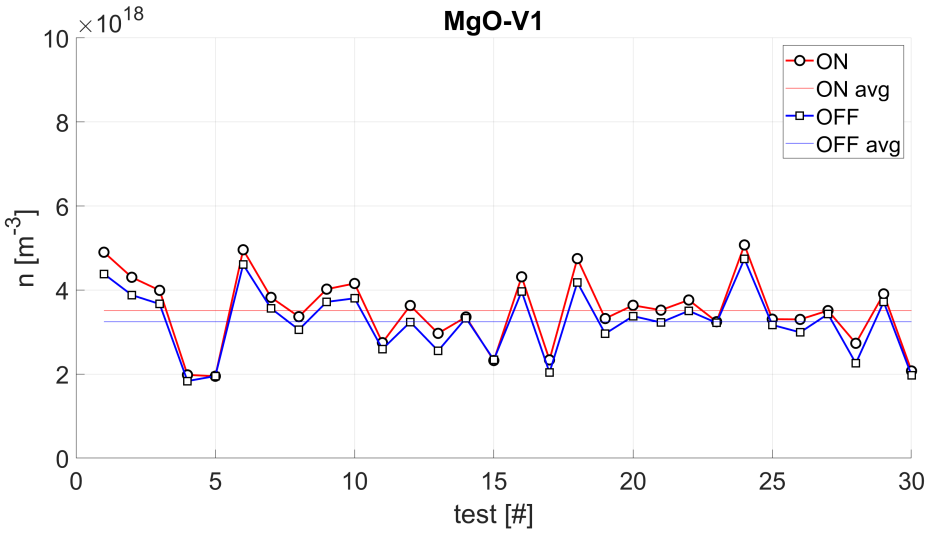

Figure 4.10: The density values of the plasma for the vessel characterized by the MgO coating with a dipping velocity (V1) of 10 cm/min for 20 seconds ON-OFF tests. X-axis reports the test sequence, Y-axis reports the density value. Measurement error on the density of $\approx$ 10 %.

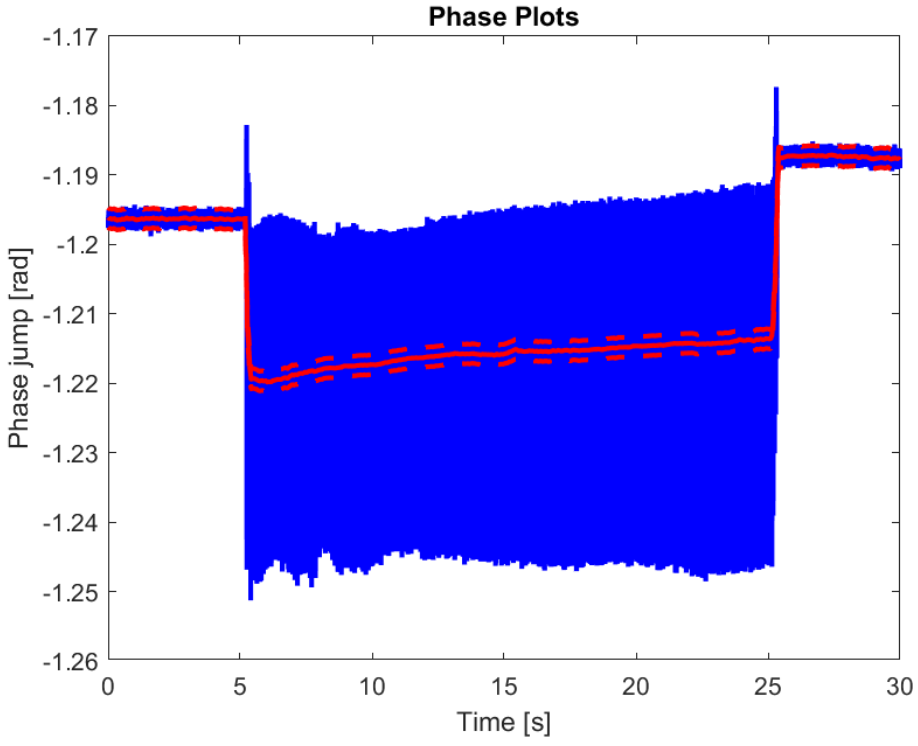

Figure 4.11: Phase plot for the vessel characterized by the MgO coating with a dipping velocity (V1) of 10 cm/min for a 30 seconds density test. Qualitative analysis of the phase jump at the beginning and end of the density test. X-axis reports the time scale, Y-axis reports the phase value.

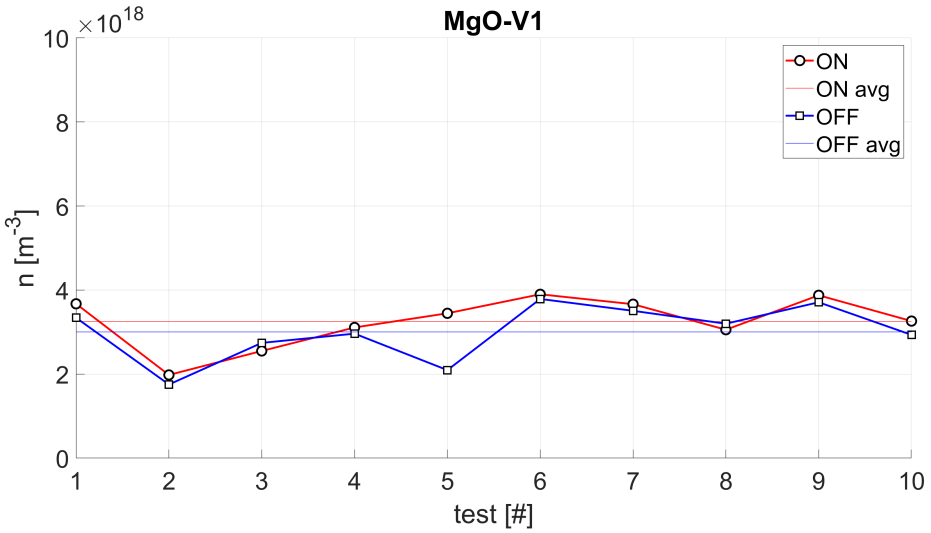

Figure 4.12: The density values of the plasma for the vessel characterized by the MgO coating with a dipping velocity (V1) of 10 cm/min for 30 seconds ON-OFF tests. X-axis reports the test sequence, Y-axis reports the density value. Measurement error on the density of $\approx$ 10 %.

4.2.3 MgO monolayer - V=20 cm/min

In this Section the tests results concerning the vessel characterized by a single layer MgO coating with a dipping velocity of 20 cm/min are shown. The phase plots and the diagrams of the plasma density are presented.

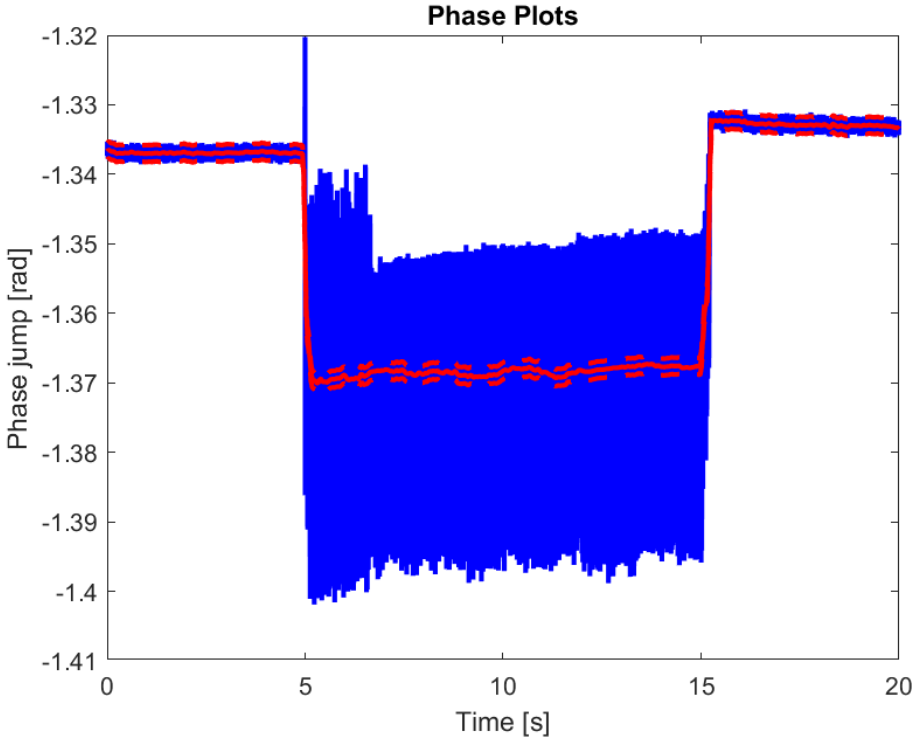

Figure 4.13: Phase plot for the vessel characterized by the MgO coating with a dipping velocity (V2) of 20 cm/min for a 20 seconds density test. Qualitative analysis of the phase jump at the beginning and end of the density test. X-axis reports the time scale, Y-axis reports the phase value.

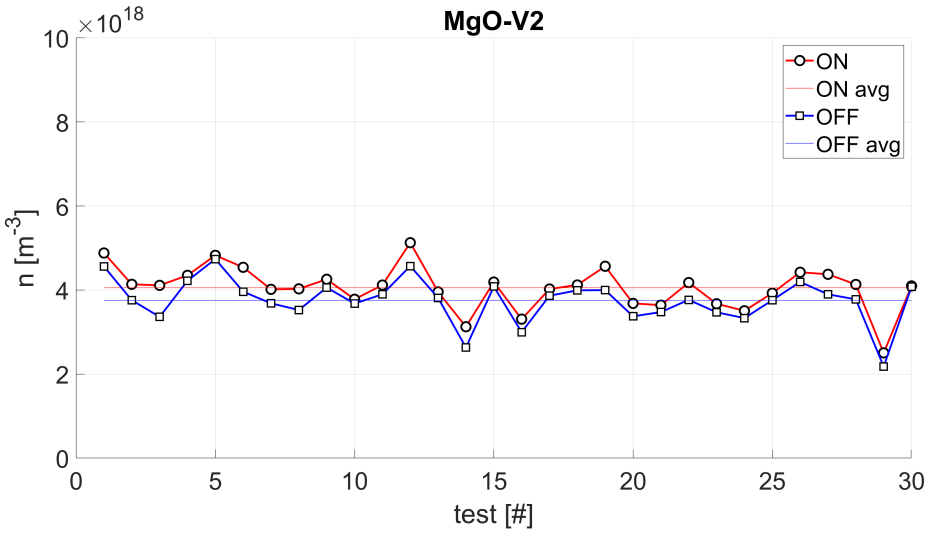

Figure 4.14: The density values of the plasma for the vessel characterized by the MgO coating with a dipping velocity (V2) of 20 cm/min for 20 seconds ON-OFF tests. X-axis reports the test sequence, Y-axis reports the density value. Measurement error on the density of $\approx$ 10 %.

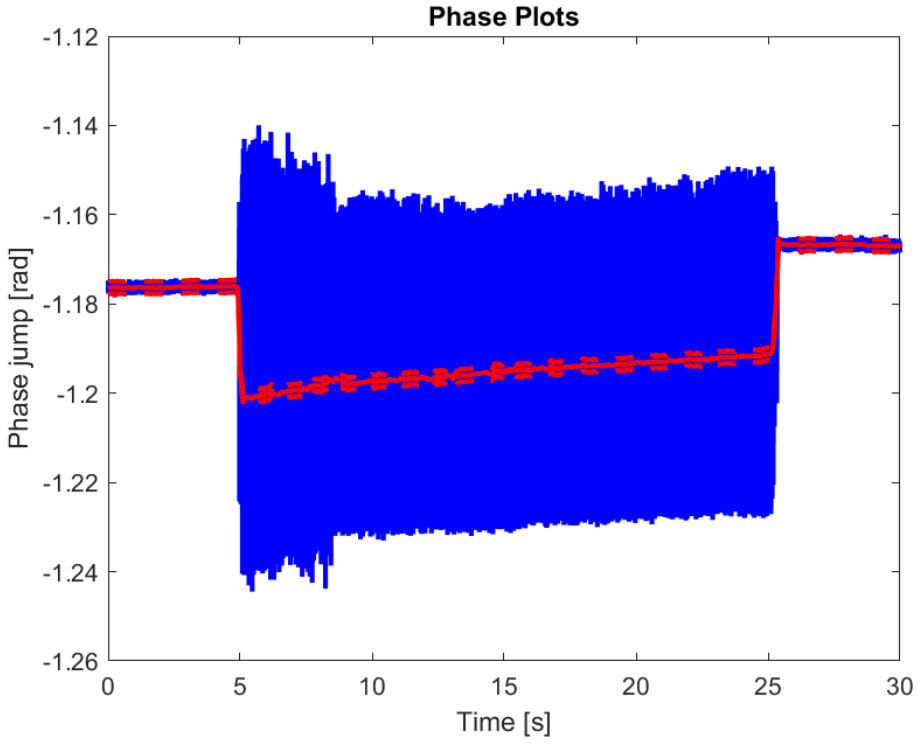

Figure 4.15: Phase plot for the vessel characterized by the MgO coating with a dipping velocity (V2) of 20 cm/min for a 30 seconds density test. Qualitative analysis of the phase jump at the beginning and end of the density test. X-axis reports the time scale, Y-axis reports the phase value.

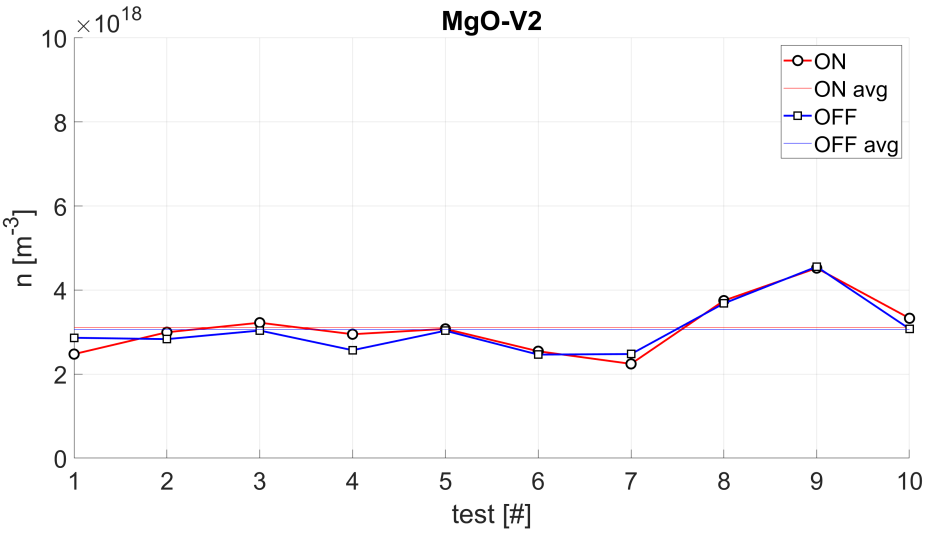

Figure 4.16: The density values of the plasma for the vessel characterized by the MgO coating with a dipping velocity (V2) of 20 cm/min for 30 seconds ON-OFF tests. X-axis reports the test sequence, Y-axis reports the density value. Measurement error on the density of $\approx$ 10 %.

4.2.4 MgO double layer

In this Section the tests results concerning the vessel characterized by a double layer MgO coating. The phase plots and the diagrams of the plasma density are presented.

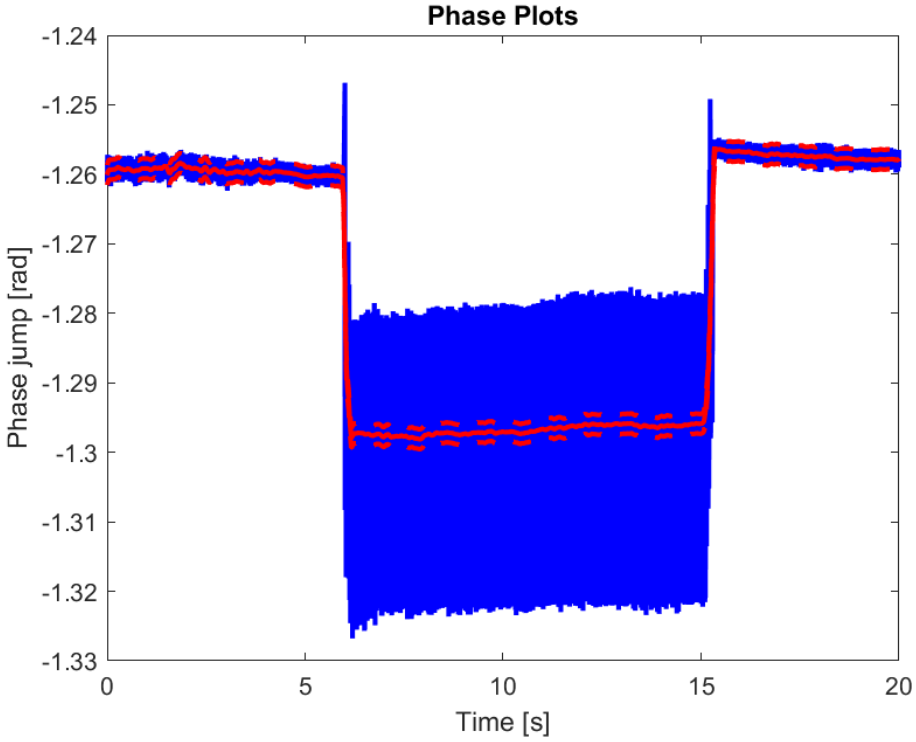

Figure 4.17: Phase plot for the vessel characterized by the double layer of MgO for a 20 seconds density test. Qualitative analysis of the phase jump at the beginning and end of the density test. X-axis reports the time scale, Y-axis reports the phase value.

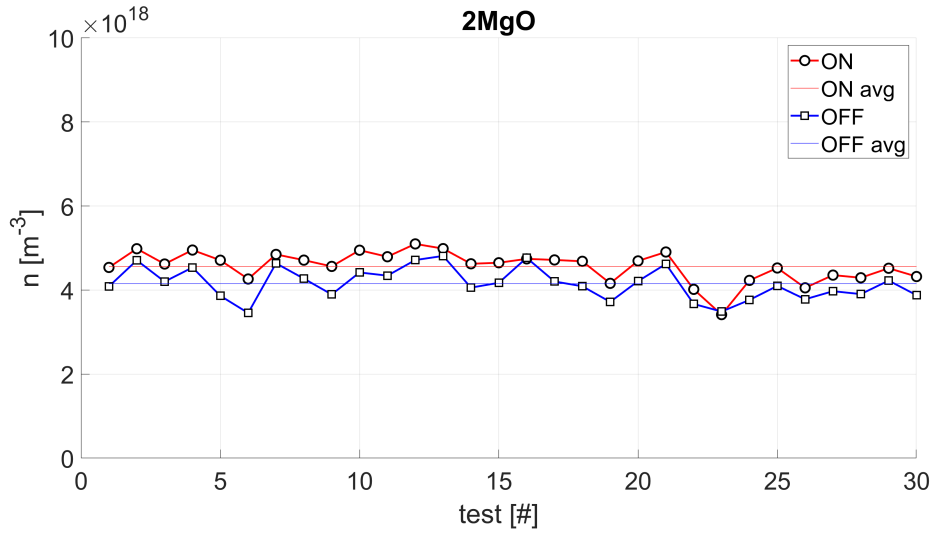

Figure 4.18: The density values of the plasma for the vessel characterized by the double layer of MgO for 20 seconds ON-OFF tests. X-axis reports the test sequence, Y-axis reports the density value. Measurement error on the density of $\approx$ 10 %.

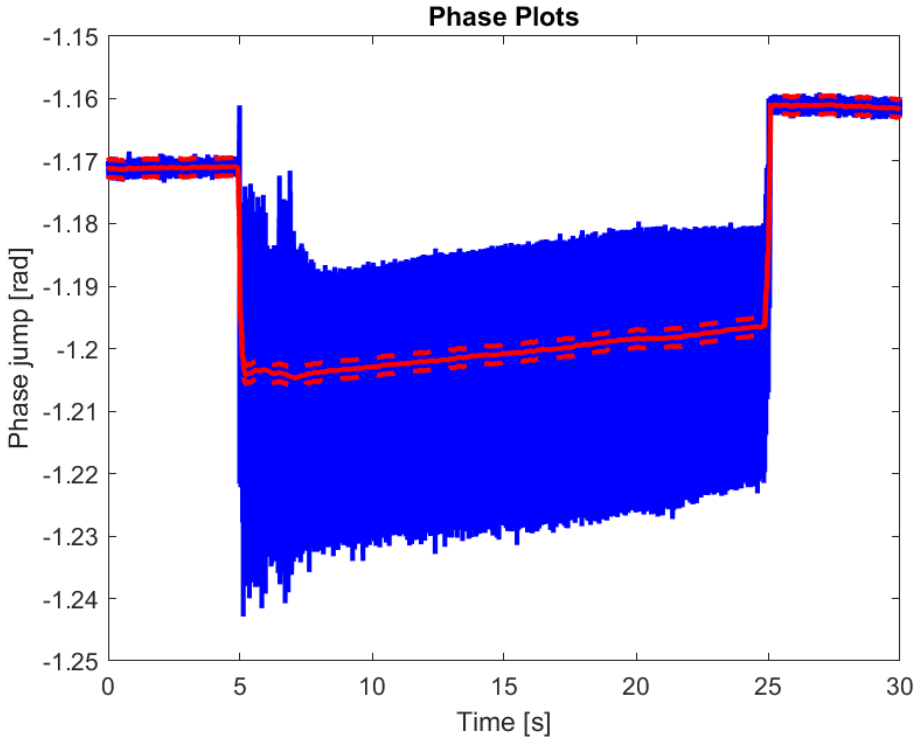

Figure 4.19: Phase plot for the vessel characterized by the double layer of MgO for a 30 seconds density test. Qualitative analysis of the phase jump at the beginning and end of the density test. X-axis reports the time scale, Y-axis reports the phase value.

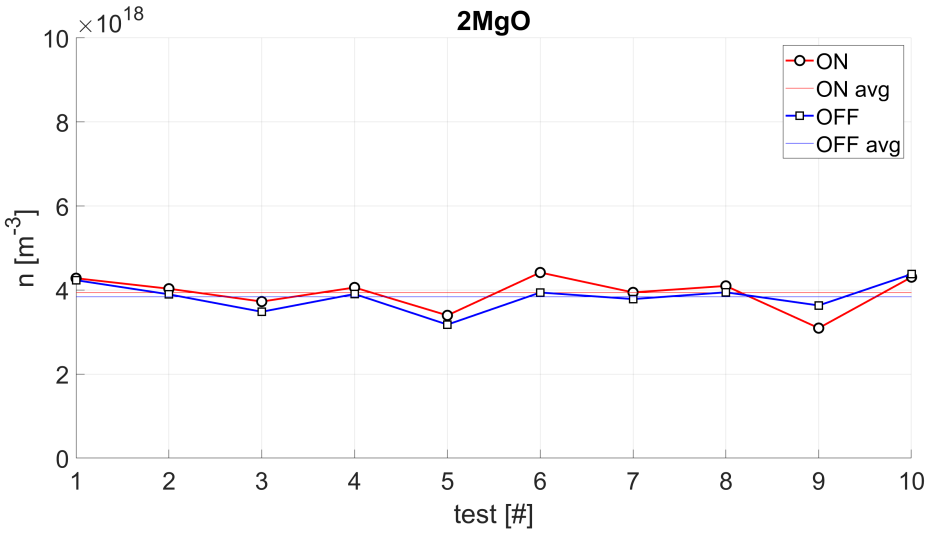

Figure 4.20: The density values of the plasma for the vessel characterized by the double layer of MgO for 30 seconds ON-OFF tests. X-axis reports the test sequence, Y-axis reports the density value. Measurement error on the density of ≈ 10 %.

4.2.5 BN layer

In this Section the tests results concerning the vessel characterized by BN coating. The phase plots and the diagrams of the plasma density are presented.

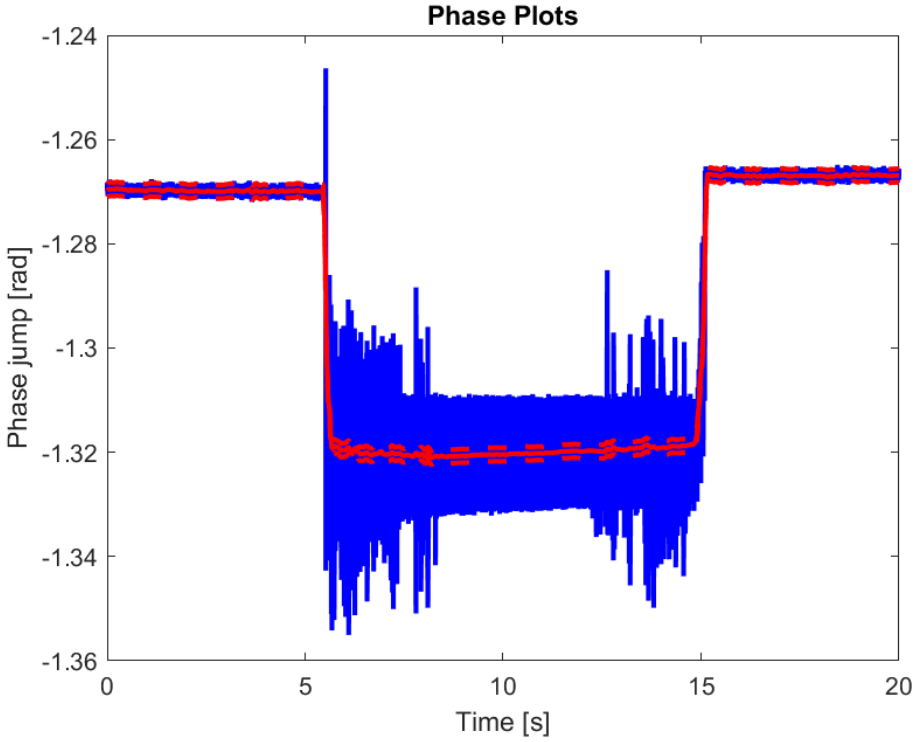

Figure 4.21: Phase plot for the vessel characterized by the coating of BN for a 20 seconds density test. Qualitative analysis of the phase jump at the beginning and end of the density test. X-axis reports the time scale, Y-axis reports the phase value.

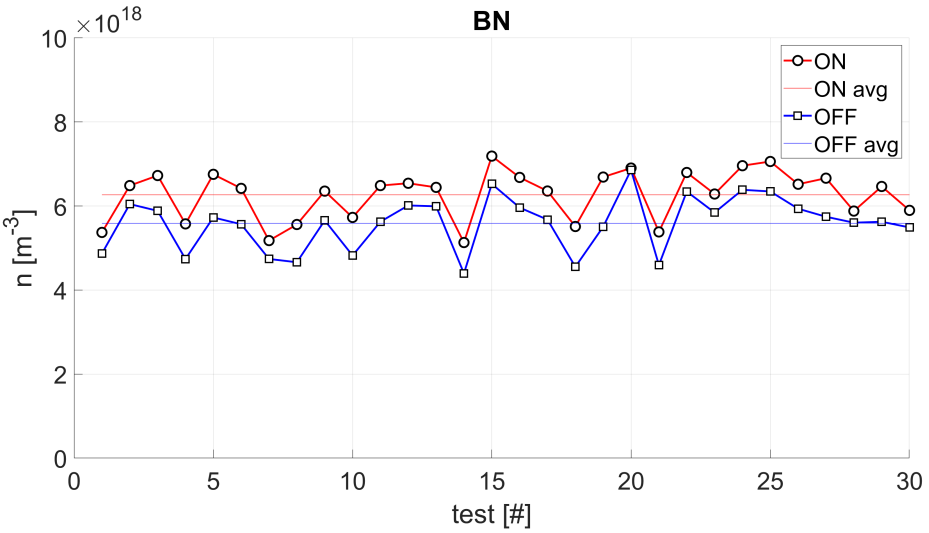

Figure 4.22: The density values of the plasma for the vessel characterized by the coating of BN for 20 seconds ON-OFF tests. X-axis reports the test sequence, Y-axis reports the density value. Measurement error on the density of $\approx$ 10 %.

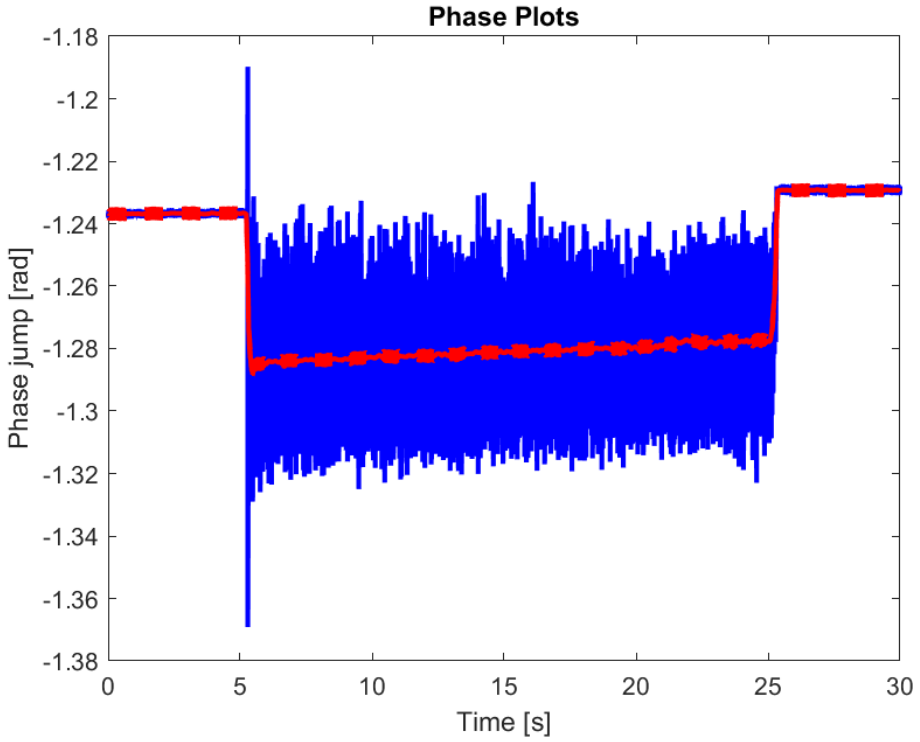

Figure 4.23: Phase plot for the vessel characterized by the coating of BN for a 30 seconds density test. Qualitative analysis of the phase jump at the beginning and end of the density test. X-axis reports the time scale, Y-axis reports the phase value.

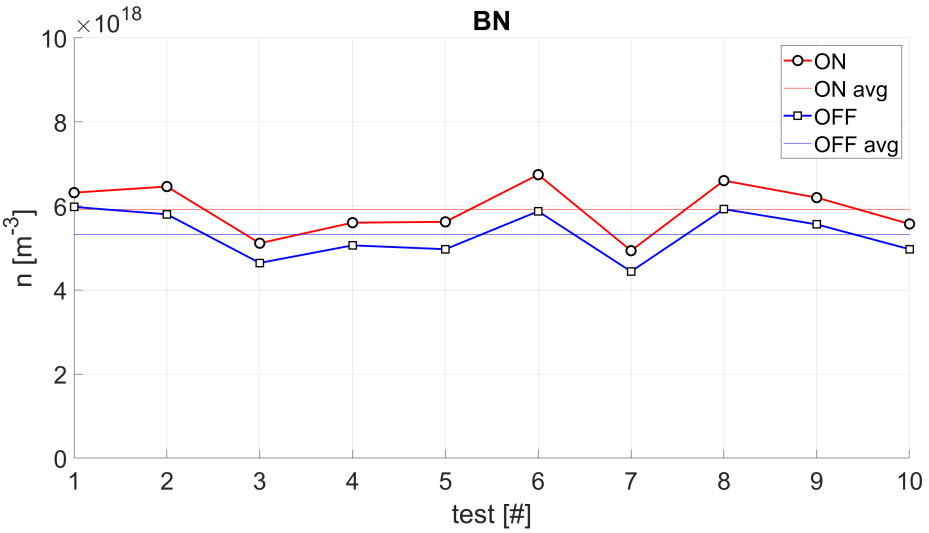

Figure 4.24: The density values of the plasma for the vessel characterized by the coating of BN for 30 seconds ON-OFF tests. X-axis reports the test sequence, Y-axis reports the density value. Measurement error on the density of ≈ 10 %.

4.2.6 Comparative analysis

In this Section the results obtained from the tests performed for the different vessels and for the duration of 20 s and 30 s are compared. In particular, this analysis is fundamental to point out possible improvement of the plasma behaviour within the vessels characterised by a coating compared to the benchmark. Moreover, the present study is essential to verify if the employment of materials with a high value of SEEY compared to the glass causes an increase of the plasma density. The Tables 4.2, 4.3, for ignition (ON) and shutdown (OFF) states, show the value of the average plasma density, the standard deviation and the relative standard deviation. The latter is evaluated by $\frac{\text{SD}}{\text{Avg density}} \cdot 100$. The results presented are respectively for 20 s and 30 s duration test.

	Avg density $[m^{-3}]$	**SD** $[m^{-3}]$	**Relative SD** [%]
Benchmark (ON)	$5.33 \cdot 10^{18}$	$9.41 \cdot 10^{17}$	17.60
Benchmark (OFF)	$4.97 \cdot 10^{18}$	$8.56 \cdot 10^{17}$	17.20
$MgO - V1$ (ON)	$3.51 \cdot 10^{18}$	$8.69 \cdot 10^{17}$	24.80
$MgO - V1$ (OFF)	$3.24 \cdot 10^{18}$	$7.87 \cdot 10^{17}$	24.3
$MgO - V2$ (ON)	$4.05 \cdot 10^{18}$	$5.26 \cdot 10^{17}$	13.00
$MgO - V2$ (OFF)	$3.76 \cdot 10^{18}$	$5.33 \cdot 10^{17}$	14.20
$2MgO$ (ON)	$4.56 \cdot 10^{18}$	$3.60 \cdot 10^{17}$	7.89
$2MgO$ (OFF)	$4.15 \cdot 10^{18}$	$3.78 \cdot 10^{17}$	9.11
BN (ON)	$6.27 \cdot 10^{18}$	$5.91 \cdot 10^{17}$	9.43
BN (OFF)	$5.59 \cdot 10^{18}$	$6.49 \cdot 10^{17}$	11.06

Table 4.2: Results for the different vessels for the 20 s duration test. The Avg density is the average plasma density, SD is the standard deviation and Relative SD is the relative standard deviation.

	Avg density $[m^{-3}]$	**SD** $[m^{-3}]$	**Relative SD** [%]
Benchmark (ON)	$4.97 \cdot 10^{18}$	$7.71 \cdot 10^{17}$	15.50
Benchmark (OFF)	$4.74 \cdot 10^{18}$	$6.36 \cdot 10^{17}$	13.40
$MgO - V1$ (ON)	$3.25 \cdot 10^{18}$	$6.11 \cdot 10^{17}$	18.80
$MgO - V1$ (OFF)	$3.00 \cdot 10^{18}$	$6.65 \cdot 10^{17}$	22.20
$MgO - V2$ (ON)	$3.11 \cdot 10^{18}$	$6.65 \cdot 10^{17}$	21.40
$MgO - V2$ (OFF)	$3.06 \cdot 10^{18}$	$6.37 \cdot 10^{17}$	20.80
$2MgO$ (ON)	$3.94 \cdot 10^{18}$	$4.19 \cdot 10^{17}$	10.70
$2MgO$ (OFF)	$3.84 \cdot 10^{18}$	$3.48 \cdot 10^{17}$	9.05
BN (ON)	$5.92 \cdot 10^{18}$	$6.33 \cdot 10^{17}$	10.70
BN (OFF)	$5.32 \cdot 10^{18}$	$5.71 \cdot 10^{17}$	10.70

Table 4.3: Results for the different vessels for the 30 s duration test. The Avg density is the average plasma density, SD is the standard deviation and Relative SD is the relative standard deviation.

As can be seen from the Table 4.2, the benchmark presents an average density plasma value of $5.33 \cdot 10^{18}$ for the ignition state and $4.97 \cdot 10^{18}$ for the shutdown state. These values are exceeded only by the plasma inside the vessel characterized by the BN coating. Indeed, it presents an average plasma density of $6.27 \cdot 10^{18}$ for the ignition state and an average plasma density of $5.59 \cdot 10^{18}$ for the shutdown state. The vessels with MgO coating show a lower average plasma density compared to the vessel made of glass. So, in these cases there is not a improvement in terms of density with respect to the benchmark. This may be due to the energy of the primary particles that hit the walls that is not sufficiently high to ensure a secondary emission. Among the vessels with the MgO coating, the vessel with the double layer of MgO presents the highest average plasma density. In fact, it has a value of $4.56 \cdot 10^{18}$ for the ignition and a value of $4.15 \cdot 10^{18}$ for the shutdown. Analysing the Table 4.3 the same conclusions have been made, with the difference that the average plasma density of the all tested cases is minor than the values obtained for the tests with a test duration time of 20 s.
In every tested case, the plasma has a constant behaviour during the time in which the vessel is in the "on" state, as can be noticed from the phase plots (Figures 4.5, 4.7, 4.9, 4.11, 4.13, 4.15, 4.17, 4.19, 4.21, 4.23).
However, in spite of the several test carried out, the density values are highly varying, as can be noticed from the diagrams of the plasma density for every test case (Figures 4.6, 4.8, 4.10, 4.12, 4.14, 4.16, 4.18, 4.20, 4.22, 4.24). This means that the plasma has not stabilized around a definite plasma density value. This behaviour is confirmed also from the Figures 4.25 and 4.26. These graphs are obtained by fitting the density values on a normal distribution curve to quickly visualize mean density and standard

deviation of each dataset, allowing for a more direct and intuitive visual inspection.

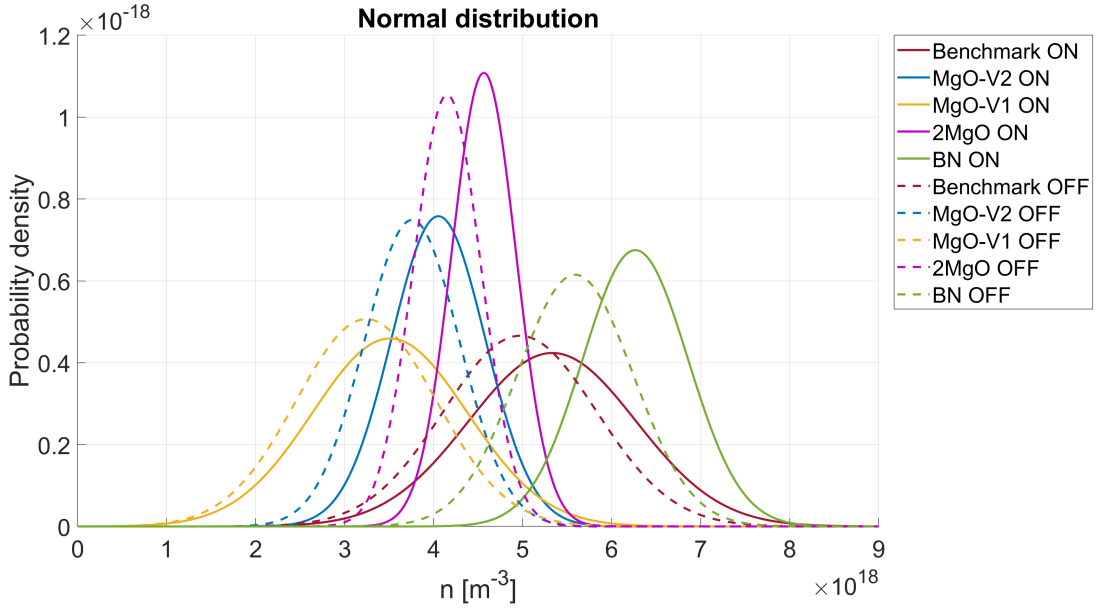

Figure 4.25: Normal distribution fit of the whole data set for the 30 s duration test, grouped by vessel name. X-axis reports the density value, Y-axis reports the probability density.

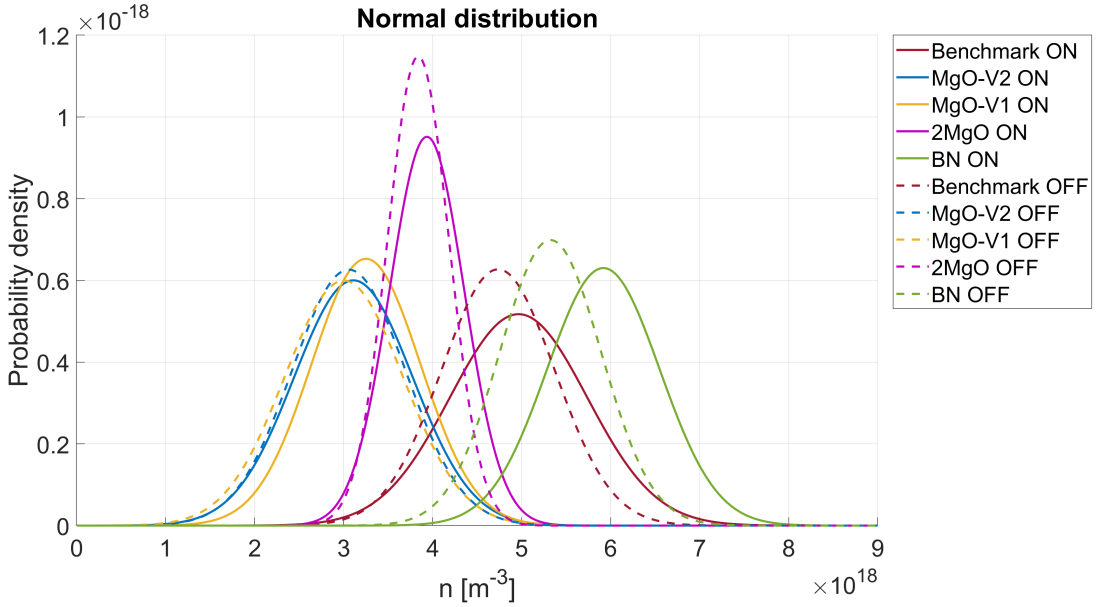

Figure 4.26: Normal distribution fit of the whole data set for the 30 s duration test, grouped by vessel name. X-axis reports the density value, Y-axis reports the probability density.

4.2.7 Degradation Test

These tests have been performed to assess the performances of the plasma discharges for longer ignitions. The density values are recorded both at the beginning and end of the measurements, so that they can be compared. The length of these tests can be set arbitrarily, depending on the needs and stability of the discharge itself. In this case the length of the tests is 90 s, 180 s and 300 s. According to the results achieved in the previous Section, the degradation tests have been done for the benchmark, the vessel characterized by the coating of BN and the vessel characterized by the double layer of MgO for 90 s duration test. Instead, on the basis of the 90 s duration test results (Figure 4.4, Table 4.27), the degradation tests of 180 s (Figure 4.5, Table 4.28) and 300 s (Figure 4.6, Table 4.29) have been done for the vessel characterized by the coating of BN and the vessel characterized by the double layer of MgO. The plots in Figures 4.4, 4.5, 4.6 show the density values across different days both for the ignition and shutdown jump allowing for a comprehensive understanding of the discharge behaviour.

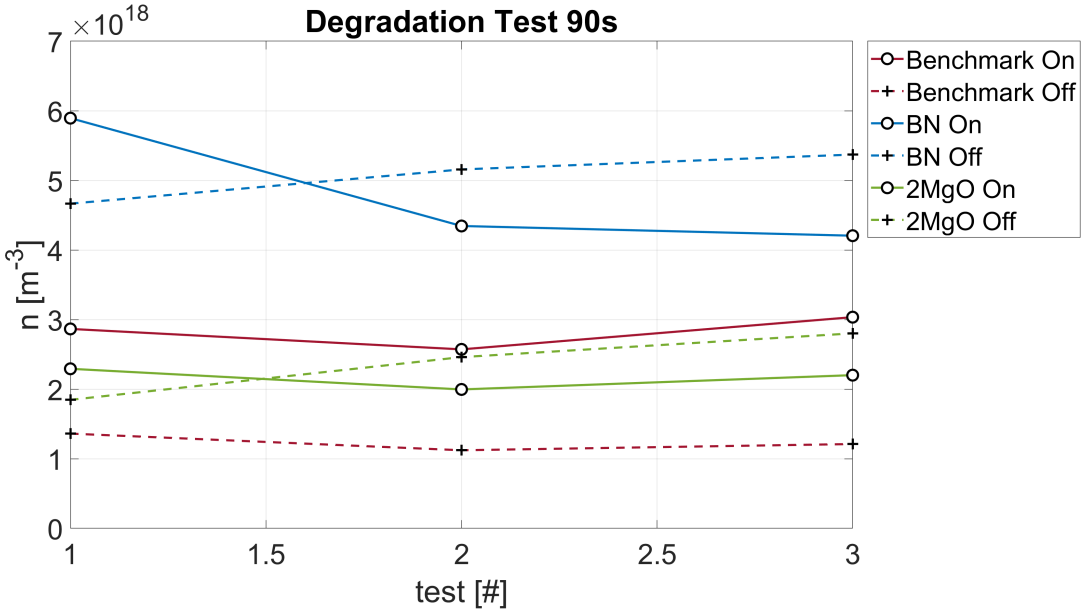

Figure 4.27: Comprehensive comparison for a 90 seconds degradation test performed on the benchmark, the vessel with the double layer MgO coating and the vessel with the BN coating. X-axis reports the test sequence, Y-axis reports the density value. Measurement error on the density of ≈ 10 %.

	Test 1 $[m^{-3}]$	**Test 2** $[m^{-3}]$	**Test 3** $[m^{-3}]$
Benchmark (ON)	$2.86 \cdot 10^{18}$	$2.57 \cdot 10^{18}$	$3.03 \cdot 10^{18}$
Benchmark (OFF)	$1.36 \cdot 10^{18}$	$1.12 \cdot 10^{17}$	$1.21 \cdot 10^{18}$
$2MgO$ (ON)	$2.29 \cdot 10^{18}$	$1.99 \cdot 10^{18}$	$2.20 \cdot 10^{18}$
$2MgO$ (OFF)	$1.85 \cdot 10^{18}$	$2.46 \cdot 10^{18}$	$2.80 \cdot 10^{18}$
BN (ON)	$5.89 \cdot 10^{18}$	$4.34 \cdot 10^{18}$	$4.20 \cdot 10^{18}$
BN (OFF)	$4.67 \cdot 10^{18}$	$5.15 \cdot 10^{18}$	$5.37 \cdot 10^{18}$

Table 4.4: Density values of ON and OFF states for the different vessels for the 90 s duration test. Three repetitions have been done.

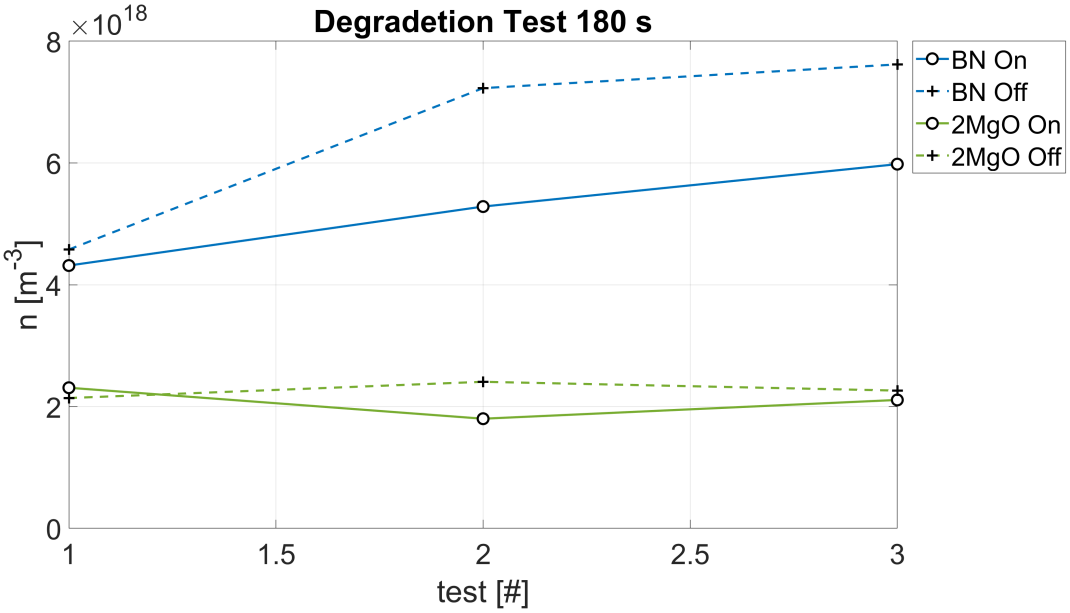

Figure 4.28: Comprehensive comparison for a 180 seconds degradation test performed on the vessel with the double layer MgO coating and the vessel with the BN coating. X-axis reports the test sequence, Y-axis reports the density value. Measurement error on the density of ≈ 10 %.

	Test 1 $[m^{-3}]$	**Test 2** $[m^{-3}]$	**Test 3** $[m^{-3}]$
$2MgO$ (ON)	$2.31 \cdot 10^{18}$	$1.80 \cdot 10^{18}$	$2.10 \cdot 10^{18}$
$2MgO$ (OFF)	$2.14 \cdot 10^{18}$	$2.41 \cdot 10^{18}$	$2.26 \cdot 10^{18}$
BN (ON)	$4.32 \cdot 10^{18}$	$5.28 \cdot 10^{18}$	$5.98 \cdot 10^{18}$
BN (OFF)	$4.58 \cdot 10^{18}$	$7.23 \cdot 10^{18}$	$7.62 \cdot 10^{18}$

Table 4.5: Density values of ON and OFF states for the different vessels for the 180 s duration test. Three repetitions have been done.

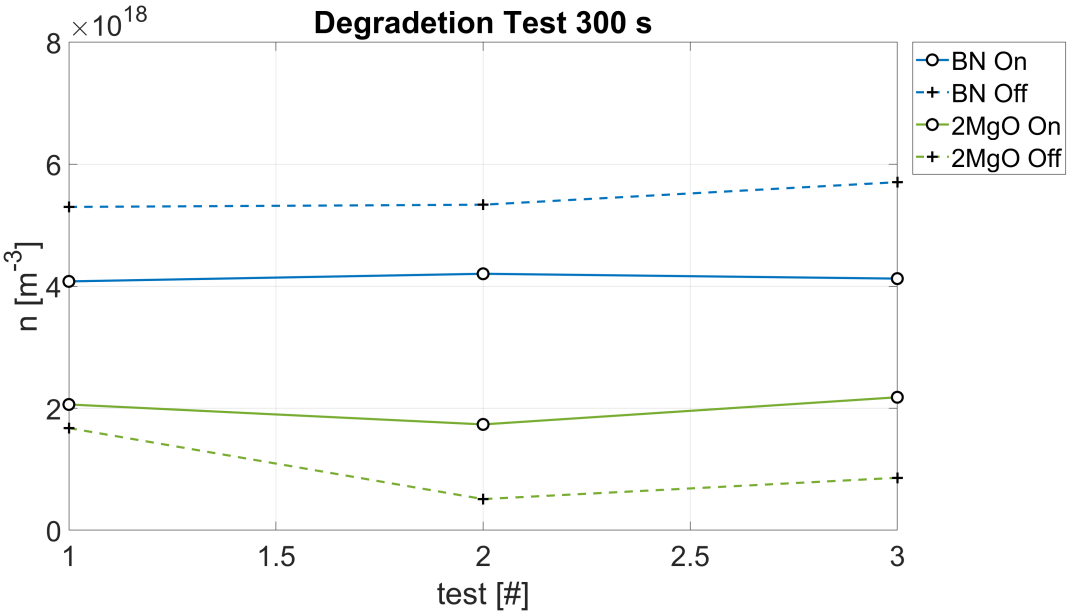

Figure 4.29: Comprehensive comparison for a 300 seconds degradation test performed on the vessel with the double layer MgO coating and the vessel with the BN coating. X-axis reports the test sequence, Y-axis reports the density value. Measurement error on the density of ≈ 10 %.

	Test 1 $[m^{-3}]$	**Test 2** $[m^{-3}]$	**Test 3** $[m^{-3}]$
$2MgO$ (ON)	$2.06 \cdot 10^{18}$	$1.73 \cdot 10^{18}$	$2.18 \cdot 10^{18}$
$2MgO$ (OFF)	$1.67 \cdot 10^{18}$	$5.10 \cdot 10^{17}$	$8.59 \cdot 10^{17}$
BN (ON)	$4.08 \cdot 10^{18}$	$4.20 \cdot 10^{18}$	$4.13 \cdot 10^{18}$
BN (OFF)	$5.30 \cdot 10^{18}$	$5.33 \cdot 10^{18}$	$5.70 \cdot 10^{18}$

Table 4.6: Density values of ON and OFF states for the different vessels for the 300 s duration test. Three repetitions have been done.

Considering the density difference between the ignition and shutdown states, shown in Figure 4.27, it can be noticed that the vessels with the coating present better performance compared to the benchmark. In fact in the latter the density difference between ON and OFF is about $1.5 \cdot 10^{18}$. For the MgO the jump is around $0.5 \cdot 10^{18}$, while for the BN is about $0.8 \cdot 10^{18}$. Also for the duration test of 180 s and 300 s the degradation of the plasma for these materials is contained, indeed as can be deduced from the Tables 4.28 e 4.29 the jump is about $1 \cdot 10^{18}$. This means that for longer ignition the performances of the plasma discharge with the coating are not significantly affected by the degradation.

CHAPTER 5

Conclusions

In this work the following topics have been addressed:

- Material selection to improve the plasma density based on a compromise between good secondary emission property and the material availability and cost;
- The deposition procedure using the sol-gel method to realize the coatings of several materials on the glass substratum. The SEM and profilometer results to analyse the thickness and the morphology of the coating have been reported;
- The realization and the test procedure of the vessel with the coating. The plasma measurement and the degradation tests results of the vessels with the coating compared to the benchmark have been shown.

Several suitable materials for the GPAs applications have been found. In particular the choice fell to MgO, Al_2O_3, TiO_2 and BN. All of these materials are used to coat the glass substratum of the cylindrical tube. MgO, Al_2O_3 and TiO_2 have been deposited using a dip-coating machinery to control the thickness. Instead, the BN has been sprayed inside the glass cylinder. Only the test results of MgO and BN have been reported. The vessels with the coating of Al_2O_3 and TiO_2 have been produced but, due to technical problems, the related test results could not be reported.

Several tests have been conducted and it was noticed that the plasma density values are highly varying for all the test cases. The highest average value for the plasma density measurement, including those that are not reported, is achieved by the BN. The degradation test results show that the vessels with the coating are not significantly affected by the degradation, compared to the benchmark. In fact, the benchmark presents already a density jump higher than the coated vessels for the test with duration of 90 s. The vessels with the double layers MgO and BN coating exhibit good performance also for ignition of 180 s and 300 s.
Considering both the density measurements and the degradation tests, the vessels

with the double layer of MgO and the sprayed BN coating present improved performance, may be due to the thickness of the layer, given that they have higher thickness with respect to the single layer of MgO.

In conclusion, adding a coating using materials with high SEEY on the glass tube, resulted in an improvement of the plasma density. Further studies on the morphology and thickness of the deposited coating are advisable, as well as exploring other methods for the deposition of the coating itself. Another possible solution could be achieved by investigating the use of adhesive ceramics in combination with Al_2O_3 or SiO_2 tubes in substitution to the glass tubes. This would allow to avoid the deposition process on the glass vessel, thus lowering the cost and complexity of the manufacture.

Bibliography

[1] Francis F Chen. *Introduction to plasma physics and controlled fusion*. Vol. 1. Springer, 1984.
Cited on pages 1, 2.

[2] Davide Melazzi, Vito Lancellotti, and Antonio-Daniele Capobianco. "Analytical and numerical study of a gaseous plasma dipole in the UHF frequency band". In: *IEEE Transactions on Antennas and Propagation* 65.12 (2017), pp. 7091–7101.
Cited on pages 3, 8, 13–15, 19.

[3] Wolfhard Möller. "Fundamentals of plasma physics". In: *University of Technology Dresden* (2014).
Cited on page 3.

[4] Boris M Smirnov. *Theory of gas discharge plasma*. Vol. 84. Springer, 2015.
Cited on page 5.

[5] Ian L Alberts, David S Barratt, and Asim K Ray. "Hollow cathode effect in cold cathode fluorescent lamps: a review". In: *Journal of display technology* 6.2 (2010), pp. 52–59.
Cited on pages 6, 15.

[6] Alexander Fridman. *Plasma chemistry*. Cambridge university press, 2008.
Cited on page 7.

[7] LF Berzak, SE Dorfman, and SP Smith. "Paschen's law in air and noble gases". In: *Lawrence Berkeley National Laboratory* (2006).
Cited on page 8.

[8] Da-Gang Fang. *Antenna theory and microstrip antennas*. CRC Press, 2017.
Cited on pages 8, 11.

[9] Constantine A Balanis. *Antenna theory: analysis and design*. John wiley & sons, 2016.
Cited on pages 9, 11.

[10] Ahmed A Kishk. "Fundamentals of antennas". In: *Ch. 1 on Antennas for Base Stat. in Wireless Comm.* (2009), pp. 1–30.
Cited on page 9.

[11] J Hettinger. "Aerial conductor for wireless signaling and other purposes". In: *Patent USA* 1309031 (1919).
Cited on page 12.

[12] Igor Alexeff et al. "Experimental and theoretical results with plasma antennas". In: *IEEE Transactions on Plasma Science* 34.2 (2006), pp. 166–172.
Cited on page 12.

[13] M Hargreave et al. "Coupling power and information to a plasma antenna". In: *AIP Conference Proceedings*. Vol. 669. 1. AIP. 2003, pp. 388–391.
Cited on page 12.

[14] GG Borg et al. "Plasmas as antennas: Theory, experiment and applications". In: *Physics of Plasmas* 7.5 (2000), pp. 2198–2202.
Cited on page 12.

[15] Gerard G Borg et al. "Application of plasma columns to radiofrequency antennas". In: *Applied physics letters* 74.22 (1999), pp. 3272–3274.
Cited on page 12.

[16] Theodore Anderson. *Plasma antennas*. Artech House, 2011.
Cited on page 13.

[17] Davide Melazzi et al. "Beam-forming capabilities of a plasma circular reflector antenna". In: *IET Microwaves, Antennas & Propagation* 12.15 (2018), pp. 2301–2306.
Cited on page 13.

[18] Giulia Mansutti et al. "L-band Plasma Turnstile Antenna for GPS applications". In: *2019 13th European Conference on Antennas and Propagation (EuCAP)*. IEEE. 2019, pp. 1–5.
Cited on page 16.

[19] A Shih et al. "Secondary electron emission from diamond surfaces". In: *Journal of applied physics* 82.4 (1997), pp. 1860–1867.
Cited on pages 19, 21, 22.

[20] KA Gschneidner. "Solid state phys. advances in research and applications (eds) F Seitz and D Turnball". In: *New York: Academic Press* 16 (1964), p. 412.
Cited on page 20.

[21] Jacques Devooght, Alain Dubus, and Jean-Claude Dehaes. "Improved age-diffusion model for low-energy electron transport in solids. I. Theory". In: *Physical Review B* 36.10 (1987), p. 5093.
Cited on page 20.

[22] Ronald Osmond Jenkins and William George Trodden. *Electron and ion emission from solids*. Dover Publications, 1965.
Cited on page 20.

[23] JR Young. "Penetration of electrons in aluminum oxide films". In: *Physical Review* 103.2 (1956), p. 292.
Cited on page 20.

[24] Cesar E Huerta and Richard E Wirz. "Surface geometry effects on secondary electron emission via Monte Carlo modeling". In: *52nd AIAA/SAE/ASEE Joint Propulsion Conference*. 2016, p. 4840.
Cited on page 20.

[25] YC Yong, JTL Thong, and JCH Phang. "Determination of secondary electron yield from insulators due to a low-kV electron beam". In: *Journal of applied physics* 84.8 (1998), pp. 4543–4548.
Cited on pages 21, 22, 26, 27.

[26] N Rey Whetten and AB Laponsky. "Secondary electron emission of single crystals of MgO". In: *Journal of Applied Physics* 28.4 (1957), pp. 515–516.
Cited on page 21.

[27] N Rey Whetten and AB Laponsky. "Secondary electron emission from MgO thin films". In: *Journal of Applied Physics* 30.3 (1959), pp. 432–435.
Cited on page 21.

[28] Yoshio Kishimoto et al. "Secondary electron emission from polymers and its application to the flexible channel electron multiplier". In: *Journal of Applied Polymer Science* 21.10 (1977), pp. 2721–2733.
Cited on page 21.

[29] H Padamsee and A Joshi. "Secondary electron emission measurements on materials used for superconducting microwave cavities". In: *Journal of Applied Physics* 50.2 (1979), pp. 1112–1115.
Cited on page 22.

[30] D Melazzi et al. "Numerical investigation into the performance of two reconfigurable gaseous plasma antennas". In: *The 8th European Conference on Antennas and Propagation (EuCAP 2014)*. IEEE. 2014, pp. 2338–2342.
Cited on page 23.

[31] Yang-Kyu Lee et al. "A new xenon plasma flat fluorescent lamp enhanced with MgO nano-crystals for liquid crystal display applications". In: *Transactions on Electrical and Electronic Materials* 11.4 (2010), pp. 186–189.
Cited on page 23.

[32] Jae-Wook Lee et al. "P-84: Cold Cathode Fluorescent Lamps with MgO-Coated Electrode". In: *SID Symposium Digest of Technical Papers*. Vol. 40. 1. Wiley Online Library. 2009, pp. 1434–1437.
Cited on page 23.

[33] Heiju Uchiike et al. "Secondary electron emission characteristics of dielectric materials in AC-operated plasma display panels". In: *IEEE Transactions on Electron Devices* 23.11 (1976), pp. 1211–1217.
Cited on page 23.

[34] Rakhwan Kim, Younghyun Kim, and Jong-Wan Park. "Improvement of secondary electron emission property of MgO protective layer for an alternating current plasma display panel by addition of TiO2". In: *Thin Solid Films* 376.1-2 (2000), pp. 183–187.

Cited on pages 24, 40.

[35] Slade J Jokela et al. "Secondary electron yield of emissive materials for large-area micro-channel plate detectors: surface composition and film thickness dependencies". In: *Physics Procedia* 37 (2012), pp. 740–747.

Cited on pages 24, 42.

[36] N Gascon, M Dudeck, and S Barral. "Wall material effects in stationary plasma thrusters. I. Parametric studies of an SPT-100". In: *Physics of Plasmas* 10.10 (2003), pp. 4123–4136.

Cited on pages 24, 25.

[37] A Dunaevsky, Y Raitses, and Nathaniel J Fisch. "Secondary electron emission from dielectric materials of a Hall thruster with segmented electrodes". In: *Physics of Plasmas* 10.6 (2003), pp. 2574–2577.

Cited on page 25.

[38] Soon Joon Rho et al. "The structural, optical and secondary electron emission properties of MgO and Mg–O–Cs thin films prepared by ion beam assisted deposition". In: *Thin Solid Films* 355 (1999), pp. 55–59.

Cited on pages 26, 40.

[39] Jeonghee Lee et al. "Thickness effect on secondary electron emission of MgO layers". In: *Applied surface science* 174.1 (2001), pp. 62–69.

Cited on pages 26, 40.

[40] Kaoru Ohya, Takayuki Itotani, and Jun Kawata. "Monte Carlo simulation of secondary electron emission from rough surface". In: *Japanese journal of applied physics* 33.2R (1994), p. 1153.

Cited on page 26.

[41] Sumio Sakka and Hiromitsu Kozuka. *Handbook of sol-gel science and technology. 1. Sol-gel processing*. Vol. 1. Springer Science & Business Media, 2005.

Cited on pages 29, 31.

[42] Alain C Pierre. *Introduction to sol-gel processing*. Vol. 1. Springer Science & Business Media, 2013.

Cited on pages 29, 30.

[43] Kiyoharu Tadanaga, Noriko Katata, and Tsutomu Minami. "Formation process of super-water-repellent Al2O3 coating films with high transparency by the sol–gel method". In: *Journal of the American Ceramic Society* 80.12 (1997), pp. 3213–3216.

Cited on pages 29, 40.

[44] Enrico Storti et al. “Preparation and morphology of magnesium borate fibers via electrospinning”. In: *Journal of the European Ceramic Society* 36.10 (2016), pp. 2593–2599.

Cited on pages 31, 34.

[45] Enrico Menin. “Sintesi di film sol-gel nanostrutturati per sensori elettrochimici ed ottici per gas inquinanti”. In: (2010).

Cited on page 34.

[46] O Tudisco et al. “A microwave interferometer for small and tenuous plasma density measurements”. In: *Review of Scientific Instruments* 84.3 (2013), p. 033505.

Cited on pages 48, 50, 51.